FUSED DEPOSITION MODELING WITH LOCALIZED PRE-DEPOSITION HEATING USING FORCED AIR

by

Seth Collins Partain

A thesis submitted in partial fulfillment
of the requirements for the degree

of

Master of Science

in

Mechanical Engineering

MONTANA STATE UNIVERSITY
Bozeman, Montana

January 2007

APPROVAL

of the thesis submitted by

Seth Collins Partain

This thesis has been read by each member of the thesis committee and has been found to be satisfactory regarding content, English usage, format, citations, bibliographic style, and consistency, and is ready for submission to the Division of Graduate Education.

Dr. Douglas Cairns, Committee Chair

Approved for the Department of Mechanical and Industrial Engineering

Dr. Christopher H. M. Jenkins, Department Head

Approved for the Division of Graduate Education

Dr. Carl A. Fox, Vice Provost

STATEMENT OF PERMISSION TO USE

In presenting this thesis in partial fulfillment of the requirements for a master's degree at Montana State University, I agree that the Library shall make it available to borrowers under the rules of the library.

If I have indicated my intention to copyright this thesis by including a copyright notice page, copying is allowable only for scholarly purposes, consistent with "fair use" as described by U.S. Copyright Law. Requests for permission for extended quotation from or reproduction of this thesis in whole or in parts may be granted only by the copyright holder.

Seth Collins Partain

January 2007

ACKNOWLEDGEMENTS

There are many people without whom this project would not have been completed. I would especially like to thank Dr. Douglas Cairns and Greg Merchant for their considerable assistance and guidance on this project. In addition, I would like to acknowledge Jay Smith, James Schmidt, Jesse Law, Pat Vowell, Dr. Alan George, Robb Larson, Dr. Ahsan Mian, and Dr. Vic Cundy for their valuable support in various aspects of this work.

I would like to dedicate this thesis to my wife, Tammy.

TABLE OF CONTENTS

TABLE OF CONTENTS - CONTINUED

LIST OF TABLES

Table Page

LIST OF FIGURES

Figure Page

LIST OF FIGURES - CONTINUED

Figure Page

LIST OF FIGURES - CONTINUED

Figure Page

ABSTRACT

Rapid prototyping (RP) systems have been used for several years to produce design prototypes without expensive tooling costs. As these systems have matured, there has been increasing interest in using them to produce actual end-use parts. Fused deposition modeling (FDM) is an RP technology that has been identified by many as having strong potential for this transition from rapid prototyping to rapid manufacturing, due primarily to its capability of using a wide array of high performance materials. FDM creates parts layer-by-layer, extruding semi-molten material "roads" through a computer-controlled nozzle onto the substrate, which is mounted on an indexing platform. This manufacturing process creates anisotropic parts, with strength properties greater along material roads than across roads or between layers.

This study proposes to improve FDM part strength in the transverse directions by increasing the amount of material bonding taking place between road and layers through the addition of a system which re-heats the substrate material immediately preceding deposition. To test this concept, a simple pre-deposition heating system (PDHS) was designed, implemented, and tested, measuring part properties in the axial and transverse directions and part dimensional accuracy. The test results were analyzed using statistical techniques, and found that parts made with the PDHS were not significantly stronger in the transverse direction than parts made without the PDHS. The development of the system and test results illustrate the challenges of implementing a PDHS system and lead to a set of recommendations for the next design iteration of PDHS.

INTRODUCTION

Rapid prototyping (RP) is a system of technologies aimed at producing physical prototypes directly from a digital design, bypassing the lengthy (and costly) traditional prototyping process—which often involves the design and fabrication of molds, jigs, and fixtures prior to actual prototype production. RP emerged in 1987 [1] and was first commercialized in 1988 with the introduction of a stereolithography (SLA) system by 3D Systems [2]. In the years that have followed, numerous systems and technologies have been introduced. The most prominent category of RP systems are known as solid freeform fabrication (SFF), of which the most common systems are known as layered manufacturing (LM) technologies, due to the way parts are created by adding material in a layer-by-layer fashion.

Most RP systems follow the same basic procedure to create parts. The procedure is as follows (See Figure 1):

1) CAD Representation – The part is designed in a solid modeling CAD package (e.g. ProEngineer© or SolidWorks©). [3]
2) Fabrication Planning – The digital representation of the part is imported into a planning software package (usually created by the manufacturer of the system), where it is "sliced" into layers for fabrication, and the tool paths and processing parameters are determined. [4]
3) Fabrication – The tool paths and processing parameters are communicated to the system and the part is created, one layer at a time. Depending on the system and

the function of the prototype, some secondary processing may be involved to improve the surface finish or remove support structures. [5]

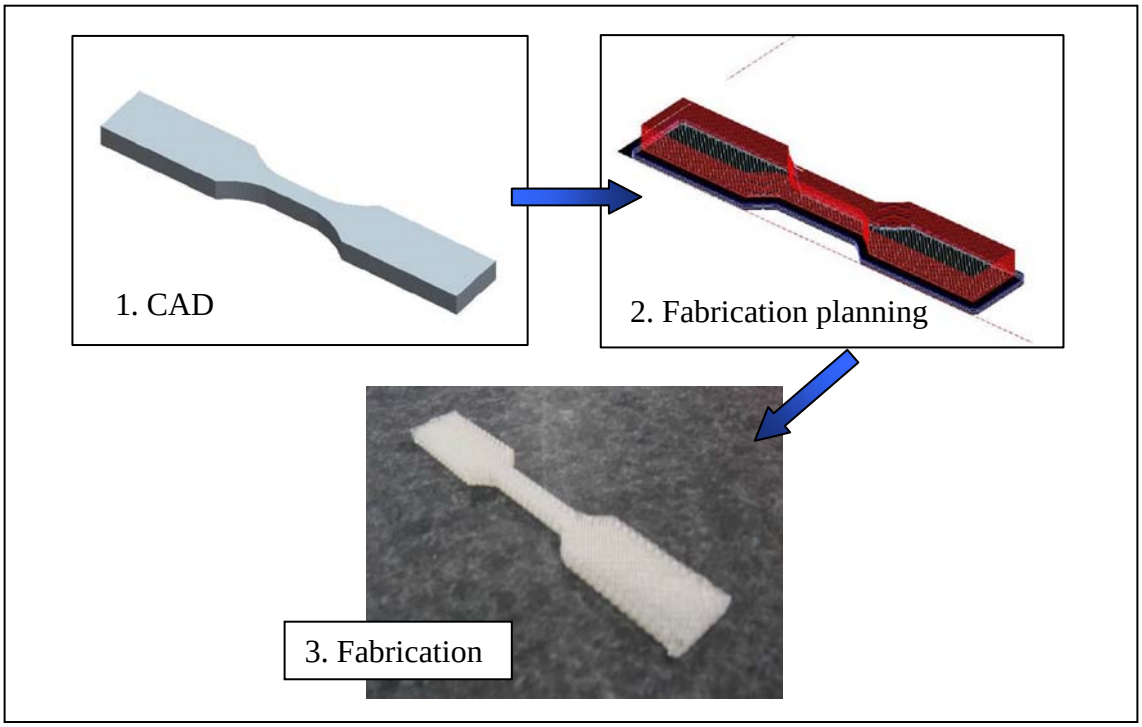

Figure 1. Procedure for rapid prototyping

As RP technologies have matured, there has been growing interest in progressing from rapid prototyping to rapid manufacturing, where parts are created for end use. Much of this interest has focused on examining existing RP systems to identify those with the greatest potential for development of a rapid manufacturing system. One of the strongest RP candidates for rapid manufacturing is fused deposition modeling (FDM). The next section contains an overview of FDM, followed by a discussion in which FDM is compared with other RP technologies.

Fused Deposition Modeling

Fused deposition modeling is a rapid prototyping technology that extrudes a semi-molten filament material through a robotically controlled nozzle. Manufactured by Stratasys Corporation©, FDM follows the basic production procedure outlined above: a solid CAD model of the part is imported into QuickSlice© (in an .stl format), the proprietary FDM planning software developed by Stratasys, where it is "sliced" into layers and a tool-path for each layer is generated. [6]. The part "slices" are determined by the software according to processing parameters entered by the user and depending on the FDM hardware being used to fabricate the part (nozzle size, material, etc.). The user-set parameters, such as row height, deposition speed, and raster angles, allow the user to tailor the fabrication to suit the needs of the part. For example, there is a "Fast Build" setting that minimizes the amount of interior material—creating a weaker part—in order to minimize the fabrication time; this option would be desirable for a user needing a quick, visual prototype where part strength and durability are not needed [7]. Within the software, tool-path planning is done in three steps: dividing the CAD model into layers (this creates a .ssl file), model material tool-path generation, and support material tool-path generation. The instructions containing the toolpath information are coded in a .sml file, which is sent to the FDM machine [8].

Once the toolpath information has been sent to the FDM machine, a filament model material (e.g. ABS plastic) is pulled by rollers into a heated liquefier, where it is melted and extruded through a nozzle onto a substrate platform. This nozzle, known as

the model material nozzle, is guided in the x-y plane and lays down the material along the model material tool-path for each layer (the extruded material is known as a “road”).

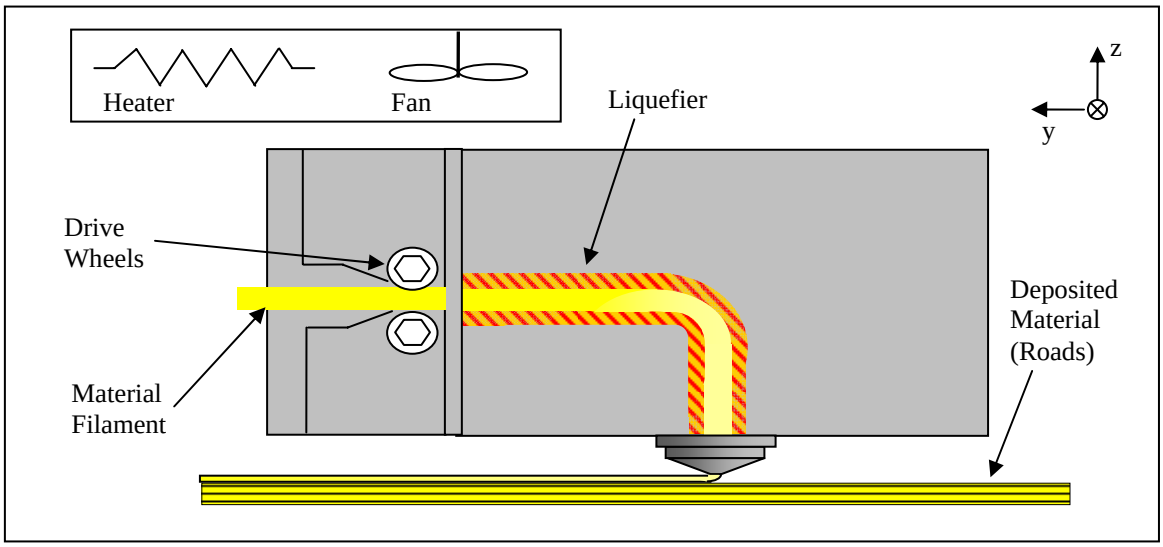

Figure 2. Fused Deposition Modeling

When one layer is complete (i.e. all of the roads planned for one level have been deposited), the substrate platform indexes in the z direction, and the nozzle lays down the next layer. That is, each layer is comprised of a sequence of roads, and the structure is built up as a sequence of layers. This process is contained within a thermally controlled environment, which is maintained to a user-set temperature. Figure 2 contains an illustration of the FDM deposition head, which guides the deposition nozzles. A support material is deposited through an adjacent nozzle (not shown in the diagram) along the support material tool-path generated by the software. The purpose of the support material is to allow for more complex shapes to be produced. Support material is manually

removed as a secondary operation. There is also a water soluble support material available that would allow the support material to be removed by soaking in a water bath.

FDM - Potential for Rapid Manufacturing

FDM has numerous strengths that make it an attractive candidate for rapid manufacturing. In order to better understand these strengths, it is useful to briefly describe two of the most popular alternatives to FDM for rapid prototyping: stereolithography and 3D printing.

1. Stereolithography (SLA) – Fabricates parts through the use of an ultraviolet laser, which hardens layers of a light-sensitive liquid resin photopolymer to form a part. These systems are manufactured by 3D Systems. [9]
2. 3D Printing (3DP) - A powdered material is distributed one thin layer at a time and selectively hardened and joined together by depositing drops of binder from an inkjet print head. For each layer, a powder hopper and roller system distributes a thin layer of powder over the top of the work tray. The inkjet nozzles than apply binder in parallel in a back-and-forth scan of the entire work area. This technology was developed at MIT in the late 1980's and commercialized by Z Corporation. [10]

The greatest advantage that FDM has over SLA and 3DP is that a wide variety of materials can be used to create parts. The first commercialized material for FDM was a grade of acrylonitrile-butadiene-styrene (ABS) plastic, but many other engineering structural materials are now available, including polycarbonate, polyphenylsulfone,

polyester, and a wax material for investment casting [11]. In addition, several studies have been conducted where FDM or modified FDM technology was used to create parts using ceramic [12], metal [13], and biomedical materials [14]. In contrast, SLA and 3DP have greater restrictions on build materials (SLA, for example, builds parts by curing a light-sensitive polymer with an ultraviolet light—so build materials must possess this light sensitivity). Since FDM can use high performance engineering materials, FDM parts are much stronger, more durable, and have greater stability (i.e. parts do not warp or curl with time or changes in environment) than parts produced using SLA or 3DP. In addition, FDM is capable of better dimensional accuracy than most other RP technologies and is cheaper to install and maintain than SLA or 3DP [15, 2].

The strengths of FDM—especially part strength, durability, and material flexibility—make a strong case for its use in rapid manufacturing compared to other RP systems. However, there are significant issues that must be resolved before FDM can make the transition to rapid manufacturing. Current FDM systems produce parts with a rougher surface finish than other RP technologies, and FDM parts often suffer from both surface defects and internal defects [16]. Another key issue is the part anisotropy that results from deposition process. Stiffness and strength are much greater along the axial direction of each deposited road than across roads or between layers, where loads are carried by the bond strength between material roads rather than the material itself. A diagram illustrating this anisotropy is shown in

Figure 3. The effects of this anisotropy can be mitigated by adjusting the part build orientation and tool-path so that the roads are oriented in the direction of part

loading, but any incidental or unforeseen transverse loads could result in the failure of the part. This anisotropy is a major concern if FDM is used

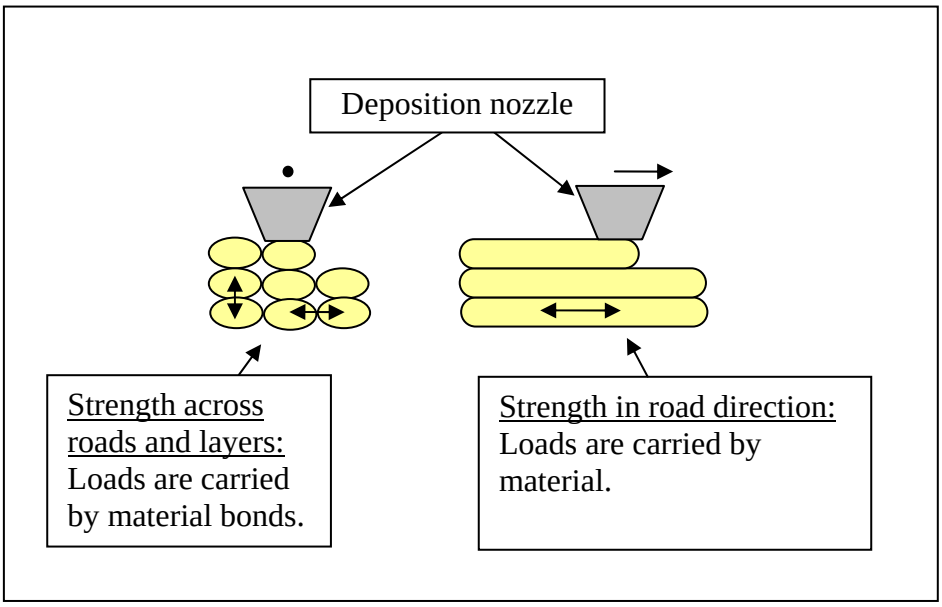

Figure 3. Anisotropy of FDM parts.

to make functional parts, and any improvements to the interlayer or inter-road bond strength will greatly improve part performance.

Literature Review

Given the potential for FDM in the field of rapid manufacturing, there have been (and continue to be) numerous studies conducted on FDM, exploring ways to use, optimize, and improve the fused deposition process to create functional parts. A large portion of this work has focused on improving part quality. Agarwala *et al.* investigated the structural quality of fused deposition ceramic and metal parts, and formulated

deposition strategies to eliminate internal and surface flaws [17]. In a similar vein, Han *et al.* developed algorithms to optimize layer evenness and quality through tool-path planning [18]. A follow-up study by Han *et al.* used similar tool-path planning algorithms to speed up part deposition without sacrificing part quality [19]. Langrana *et al.* developed a virtual simulation and video microscopy system to monitor the quality of FDM parts in real time [20]. Anitha *et al.* studied part quality from the standpoint of surface finish (rather than the presence of defects) using a statistical analysis of variation which measured the effects of processing parameters on surface roughness [21].

Another section of work has focused on innovative applications and materials for FDM. Bose *et al.* and Darsell *et al.* both explore the use of FDM in producing scaffold structures for biomedical applications [22, 23]. Shofner *et al.* developed a nanofiber-reinforced ABS feedstock material for FDM, which resulted in significant increases in part stiffness and strength [24]. Bellini *et al.* and Wu *et al.* report on significant work by a research group based at Rutgers University, exploring the use of fused deposition technology to produce functional ceramic and metallic parts [12, 25]. Yan *et al.* use fused deposition technology with biomaterials to create scaffolding for organ regeneration [26].

Finally, much of the current literature addresses characterization, modeling, and optimization of FD part stiffness and strength. Bellini and Güçeri characterized FDM parts by modeling the parts as an orthotropic material and conducting tensile tests to determine the appropriate material constants [27]. Rodriguez, Thomas, *et al.* produced a series of articles resulting from an extensive research program aimed at developing a

design tool for optimizing the mechanical performance of parts produced using fused deposition. This study included a characterization of the microstructure [28] and mesostructure [29] of fused deposition ABS (FD-ABS) parts, an investigation of bond strength in FD-ABS parts [30], the development of a model to predict the stiffness and strength of FD-ABS parts [31], and the development of an optimization algorithm, which incorporates the previous work to maximize part performance [32]. Kulkarni and Dutta examined the effects of deposition strategies on FDM part stiffness and used laminate theory to model the stiffness of FDM parts produced using a raster tool-path [33]. Yan *et al.* conducted a study analyzing bond strength in fused deposition wax parts as a function of processing parameters and developed a variable, bonding potential, to measure the bonding interface status [34].

This review of the literature illustrates a gap in the discussion of improving FD part strength in the transverse direction. The majority of the current literature looking to improve FDM part performance does so from the standpoint of either tool-path planning or enhanced materials, rather than hardware or deposition process improvements. Of the articles reviewed above, only two (Rodriguez *et al.* [30] and Yan *et al.* [34]) address interlayer part strength directly. Both of these studies explore bond strength or bond toughness as a function of the existing hardware and process parameters, seeking to both characterize and optimize interlayer and inter-road strength. The findings of these studies illustrate the processing parameters critical to developing strong material bonds. The next section contains a discussion of the bonding process that occurs during fused deposition modeling, which draws upon these works to set up the goal of this research.

Description of Bonding Process

The deposition process used by FDM to fabricate parts—bonding polymer roads and layers to create the part geometry—is essentially an extension of thermoplastic welding. The bonds created during such a process are formed through molecular bonding via the interpenetration of molecular chains across a bonding interface. As this interpenetration increases, the interface gradually disappears and bond strength develops. This process is a type of mass diffusion and is thermally activated, only occurring at temperatures above a critical temperature, T_c. There is a slight disagreement in the literature about this critical temperature: Rodriguez *et al.* use the glass transition temperature, T_g [37], while Yan *et al.* use the Vicat softening temperature as the critical bonding temperature [38]. In this work, this disagreement regarding which material paramter is the critical temperature is relatively unimportant—the material under investigation is an amorphous polymer (ABSi 500), so the values for the glass transition temperature and the Vicat softening temperature are relatively close together (94^0 C and 98-100^0 C, respectively [37,39]).

Yan *et al.* describes the molecular diffusion process occurring in FDM using the following Arrhenius form of the diffusion equation:

$$dm = -D_0 e^{-Q/RT} \frac{dc}{dx} dt \qquad (1)$$

Where:
D_0 = Diffusivity constant of the system
T = Interface temperature
Q = Activation energy of the diffusion material
c = Concentration of diffusion material
x = Diffusion distance

R = Gas constant

The concentration gradient dc/dx changes in a complicated fashion, making it difficult in practice to accurately measure or calculate the interface bonding status with the accurate amount of diffusion. To allow for more practical measuring of the bonding interface status, Yan *et al.* introduced variable called bonding potential (ψ), defined as follows [38]:

$$\psi = \int_0^{\infty} \xi(T) \cdot e^{-k/t} dt$$
$$\xi(T) = \begin{cases} 1 & T \geq T_c \\ 0 & T < T_c \end{cases} \qquad (2)$$

Where: T_c = Critical bonding temperature
k = Bonding potential coefficient (units in temperature)
T = Interface temperature

The higher the bonding potential, the greater the degree of bonding and the stronger the bonds become. Yan and coworkers used finite difference methods to calculate the bonding potential for different processing conditions (envelope temperature, nozzle temperature, etc.) and performed tensile tests to correlate bonding potential with part strength.

Rodriguez *et al.* characterized the molecular diffusion as having three stages: wetting, diffusion, and randomization. During the wetting stage, inhomogeneities on the surface—which act as barriers to molecular interpenetration—disappear, which allows molecular chains to move freely across the surface. At temperatures much greater than T_g, wetting is assumed to happen instantaneously. Diffusion and randomization are

described by the reptation model introduced by De Gennes, where polymer molecules move and back and forth along their backbones in a snake-like Brownian motion [40]. Rodriguez *et al.* draw from reptation theory to derive an expression for the normalized interface toughness of a FDM bond that assumes instantaneous wetting, that the toughness of the bond is proportional to the monomer segment interpenetration depth across the interface, and a time-dependant interface temperature [37]:

$$\frac{K(t)}{K_\infty} = \frac{K_0(T)}{K_\infty} + \left[\frac{1}{t} \int_0^t \left(\frac{\tau}{C \exp\left(\frac{Q}{RT(\tau)}\right)} \right) d\tau \right]^{1/4} \qquad (4)$$

Where: K = toughness of interface material
K_∞= maximum toughness (equal to the toughness of the virgin material)
$K_0(T)$ = toughness that occurs due to surface wetting only (no interdiffusion)
T = interface temperature
t = time that T is greater than T_g
Q = material activation energy
R = gas constant
C = pre-exponential factor, assumed constant

In a similar vein as Yan *et al.*, Rodriguez and coworkers used a finite element model to calculate the time-dependent interface temperature $T(\tau)$, and used (4) to predict the interlayer toughness of FDM parts. They created several FDM fracture toughness samples with different processing parameters and compared the model predictions with the test results.

All of the expressions noted here that describe the bonding process demonstrate that the critical factor in establishing good bonding between material roads is the

interface temperature—the longer the interface temperature is above the critical temperature, the greater the strength of the material bond. The results of the two studies examined here reflect this relationship. Both found that the process parameters most critical to the interlayer bond strength or toughness were those that affected the interface temperature: the envelope temperature, T_e, and the convection constant, h, within the envelope. These parameters control the rate of cooling of a newly deposited road or layer, which becomes the substrate for the next layer or road. The nozzle temperature, T_n, also plays a role in bond strength as it controls the amount of energy transferred to the road/base system, but both studies found that T_e affected bond strength more than T_n. Rodriguez *et al.* determined that the parts created at $T_e = 158^0$ F (70^0 C), the highest envelope temperature the machine is capable of maintaining, had the best interlayer performance.

The findings of these studies have large ramifications on the use of FDM for rapid manufacturing. The dependence of bond strength on maintaining a high environment temperature and low convection constant, as in the current process, would make it necessary to keep the deposition environment in an insulated, thermally controlled envelope. This envelope then becomes a constraint on the size of part that can be produced. In addition, the interlayer strength will vary due to the size of the part being fabricated: large parts require more time between layers than small parts, which allows the substrate more time to cool between layers and will result in weaker interlayer strength.

Goals Of The Thesis

The goal of this research was to develop a system to heat the substrate material prior to deposition. This heating process is designed to raise the interface temperature above the critical level where bonding occurs, increasing both the degree of to which bonding occurs and the strength of these bonds, resulting in greater transverse strength in FD-ABS parts. Although it is impossible to anticipate all of the ramifications of adding this additional heat to the process, there are two potential adverse effects that are immediately identifiable. The first is that excessive heat can cause degradation and material instability of the feedstock material, leading to a loss of properties. The other is that maintaining the part at too high of a temperature may prevent the material from solidifying enough to support additional layers, causing the part to slump and damaging the dimensional accuracy of the process. With these considerations in mind, the work was divided into two phases: design and implementation of a Pre-Deposition Heating System (PDHS) and analysis of the system through statistical methods.

The remainder of this thesis contains a description of the procedure and results of the two work phases listed above. A description of the pre-deposition heating system, including the design considerations, system development, and limitations is given in the next chapter. A discussion follows on the experimental design and testing procedure for analyzing the effects of the pre-deposition heat system. Finally, the results are discussed and recommendations are made for additional work in this area.

PRE-DEPOSITION HEATING SYSTEM

Requirements & Considerations

The first task of designing the PDHS was to develop a set of system requirements and considerations, which would guide the selection of the system components. These requirements are listed below.

1. The PDHS should able to heat the substrate at least 90^0 C (194^0 F), the estimated glass transition temperature of the ABS material [39], and preferably up to 270^0 C (518^0 F), the optimum nozzle temperature and point at which the material is molten [42].
2. The PDHS should accomplish substrate heating without contact, to keep from disrupting the material.
3. The PDHS should apply substrate heating in as localized an area as possible. This requirement stems from several considerations. Applying heat in a general sense is not conceptually different from the current system—which includes a control that automatically shuts the machine down if the environment temperature goes above 75^0 C (167^0 F). Also, heating the entire part to the critical temperature at which bonding occurs would seriously degrade the dimensional accuracy of the part.
4. The PDHS should be a separate, non-intrusive system from the FDM machine. The FDM machine used in this work is an important learning tool that is frequently used by students and faculty at Montana State University, and this

requirement was out of consideration to those users. Essentially, this requirement means that the system must be implemented without drilling holes or otherwise permanently modifying the FDM machine. This work is a proof of concept, and so the PDHS must be able to be removed from the FDM machine at its conclusion.

The next section contains a discussion of the technologies that were investigated as the basis for the PDHS, and how the list of requirements listed above was used to select the technology for the system.

System Alternatives

Several different systems were considered for accomplishing the substrate heating, based on the requirements listed in the previous section. Since the bonds between layers in FDM are essentially welded bonds, the search for candidate systems revolved around plastic welding technologies. The "no-contact" requirement limited the field to three basic technologies: laser welding, ultrasonic welding, and forced air welding. Each of these systems will be discussed.

Laser welding systems were first commercialized in the 1970's, and are now used in many industrial applications. Two forms of laser welding are generally used for polymers: CO_2 and transmission welding (Nd:YAG). Transmission welding requires a transparent and colored pairing of materials, which does not apply in this situation. CO_2 welding is more applicable for this application. The major advantage of a laser welding system is its ability to precisely deliver a controlled amount of heat to a localized point.

Some disadvantages for this technology are the amount of hardware required (optics, cooling system, power source, etc), which would require extensive customization to adapt it for this purpose. Also, these systems are usually designed for mass production, so the costs can be considerable [43].

Ultrasonic welding systems use ultrasonic waves to vibrate and melt the material at the weld line. A transducer creates the waves, which are then transmitted via a booster/horn assembly attached to the transducer. This technology is a non-contact method of welding, but usually requires the parts to be welded to be clamped together (before, during, and after the welding process). This need for clamping does not fit this application, as the top layer will be semi-molten. Also, similar to the laser welding systems, this technology is usually intended for mass production and equipment and operating costs can be considerable [44].

There are several applications where forced air is used to dry or heat a base material, including thermoplastic welding. The advantages of these systems are that they are low-cost and simple, allowing for easy adaptability. Several different devices were investigated for use in this application, including heat guns, hot air pens (for electronics rework), and thermoplastic welding units. The major disadvantages of these systems is in the application of the heat, which is not as controlled or localized as the other systems.

Based on the investigations into potential heat systems, the forced air systems were the best option for this work due to their availability, cost, and ease of adaptation. The laser welding systems had the most desirable heating qualities, but the cost and effort

of implementation were beyond the scope of this work. The following sections discuss the development of the system, beginning with the selection of the heating system.

Heating System

As discussed in the previous section, several different types of forced air heater were investigated. The heat range requirement proved to be a major factor in finding a suitable heater, as most of the readily available heat guns (for painting applications, etc) do not heat to 270^0 F. Other desirable factors were adjustability of temperature and air flow, and anticipated ease of integration with the FDM system. The heater selected for the PDHS system was a PVC welding kit made by Chicago Electric Power Tools© (see Appendix A for product information). The welder is a hand-held unit that heats compressed air supplied through a flexible integrated power/air cord specifically designed to weld thermoplastics.

The manual for the welder lists a maximum temperature of 600^0 F (315.5^0 C), which satisfies the temperature requirement. However, the welder does not have any controls that allow the user to adjust the temperature. To address this, a Variac© variable transformer was obtained and used to regulate the voltage supplied to the welder, which in turn controls the temperature [45]. In addition, a valve was attached between the compressed air supply and the welder which allows the user to adjust the air flow.

To evaluate the performance of the welder, a temperature test was conducted. The welder was run for three hours (the upper limit to the test sample run time, described

in the next chapter) at full power with the air valve open, with a thermocouple positioned close to the output nozzle of the welder to measure the air temperature (see Figure 4).

Figure 4. PVC welder temperature test setup

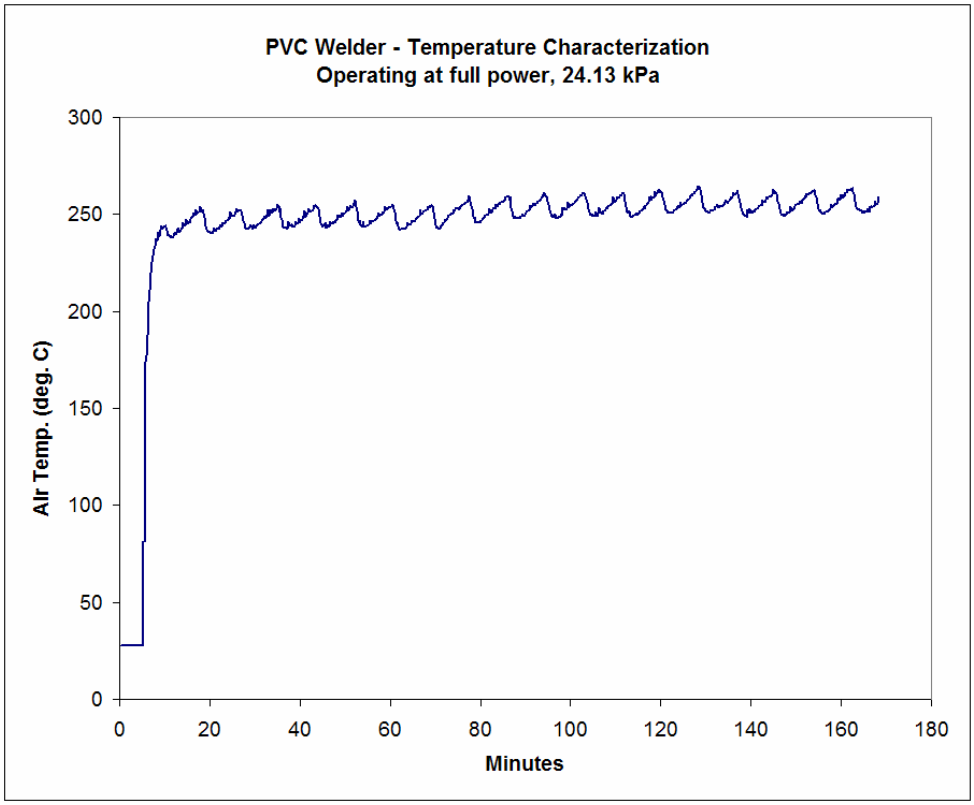

Figure 5. Temperature test results for welder at full power

The results of the test showed that after a warm-up time of approximately 10 minutes, the air temperature fluctuates in an approximately periodic way: cycling approximately every 8 minutes between a maximum temperature of 262.9^0 C and a minimum temperature of 240.3^0 C, with an average temperature of 250.9^0 C (see Figure 5). The fluctuation is most likely caused by temperature controls in the welder, which would explain its cyclic nature. The amount of fluctuation in temperature was disappointing, since it is desirable to keep the temperature as constant as possible. As a result, for the purposes of the experiment, the voltage will be used as the factor controlling temperature (since it can be set at a constant level by the user) and it will be recognized that each voltage produces a range of air temperatures, rather than a single constant temperature. This temperature resolution is not ideal, but will serve for the purpose of satisfying the goal of this thesis, which is to investigate the effects of pre-deposition heating in a general sense (rather than optimizing the air temperature).

Mounting and Heat Delivery Hardware: Welder to the Deposition Head

Once the heating component of the PDHS was selected, the next step was to develop the hardware for mounting the components in the desired locations and delivering the heated air to the desired location in front of the nozzle. There are two stages of heat delivery: delivering the air from the heater to the deposition head, and delivering the air from the deposition head to the point of application in front of the material nozzle. The hardware development of each of these stages will be discussed separately.

The initial design of the system was to keep the PVC welder outside of the FDM enclosure so that it could be monitored easily, and use hose to run the air from the welder to the deposition head. The hose had to be flexible to allow for free movement of the deposition head. In addition, the distance from the PVC welder (assuming that it would be mounted to the back of the FDM) to the deposition head, with enough slack to allow for the deposition head to reach any point in the enclosure, was measured at 1.54 m (the best access to the deposition head is through a door on the back of the enclosure). Thus, the requirements for the hose were flexibility, capability of withstanding air heated to temperatures in excess of 270^0 C, and a 1.54 m length.

After some research, it was determined that the best option for the hose was 0.635 cm 304 SS braided hose, which was the most flexible hose found that was still capable of handling the high temperatures of air. The nozzle on the PVC welder unscrews, allowing hose with a 0.635 cm NPT male fitting to be screwed directly to the welder. A 1.54 m length of the hose with the appropriate fittings was purchased and attached to the PVC welder. To prevent heat loss, the hose was wrapped with fiberglass insulation tape. The welder was run at full power for several hours, and the air temperature at the hose outlet was monitored. However, the temperature of the air never rose above 70^0 C, which was deemed unacceptable for this application. The cause for the reduction in air temperature was most likely due to convective cooling in the hose.

The results of testing the flexible hose led to the conclusion that heater must be as close to the point of application as possible, to minimize the amount of heat lost during transit. Therefore, it was decided to mount the PVC welder directly to the deposition

head. The cord supplying the power and air to the welder is 3.65 m long and flexible, easily allowing for deposition head movement. Once this was decided, the next step was to design a frame for mounting the welder.

The first step in designing the frame to fix the welder to the deposition head was to determine the mounting location. The diameter of the welder eliminates mounting it to the underside of the head, as there would be insufficient clearance. Likewise, the rails on which the head is mounted would obstruct the welder if it was mounted to the top. Between the two sides, the right side has more hardware and wiring, whereas the left side is clear except for a buckle, which sticks out about .012 m from the side of the head. Therefore, it was decided to mount the welder on the left side. An aluminum plate was cut to the length of the deposition head, and six bolts with aluminum spacers were mounted around the edges of the frame to allow the frame to clear the buckle on the side.

The next step was to determine both how to rigidly fix the frame onto the deposition head, and how to locate the frame on the deposition head so that it could be removed and reattached in the same place. In keeping with the system requirements listed previously, this had to be accomplished without drilling holes or otherwise permanently altering the deposition head. In the first iteration of the design, a through hole found in the section of the deposition head hardware used to mount the head onto the overhead rails, towards the front of the head. This hole provided a means of both locating the frame and supporting the frame in the vertical direction: two bolts with threaded 0.635 cm nylon spacers were mounted to the frame, one to fit into the hole in the front, the other to rest on the top of the head in the rear.

At this point, the frame could rest in position to the deposition head, but was not securely fastened to it. To accomplish this, some means of strapping the frame onto the deposition head needed to be added. The first solution was to use a simple bungee cord to hold the frame firmly against the side of the head. However, during one of the trial runs of the system, the bungee cord was used to wrap the entire assembly (welder and frame) to the head, and it pressed too tightly against the rubber grip of the welder. This caused the grip to come into contact with the heating element, which melted both the rubber and bungee cord before the system was turned off. The next solution was to use hook-and-eye strapping material to secure the frame to the head, which has the added benefit of ease of use in attaching and un-attaching the frame.

With a frame in place, the next step was to devise the means of mounting the welder to the frame. The simplest solution was to use a pair of grip clips, commonly used to hang brooms and mops. These clamps held the welder firmly in place, but also allowed the welder to be pulled out easily, if the need arose. For additional security, a strip of hook-and-eye material was added to each clamp to hold the welder in place (see Figure 6).

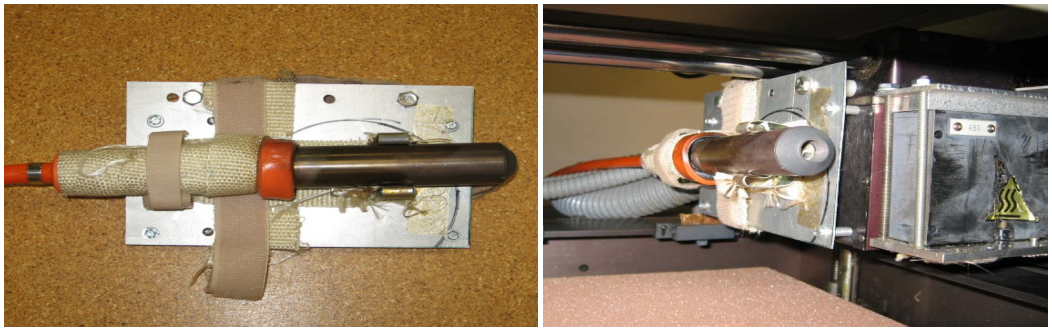

Figure 6. Welder and frame, unmounted and mounted configurations.

At this point in the design, the welder could be attached to the deposition head securely. However, there is one aspect of the system that is worth noting. The procedure for running a part on the FDM begins by "Sending" the part to the machine, at which point the machine goes through a "homing" procedure—during which the deposition head travels to the front left corner of the enclosure. After completing this procedure, the machine pauses, allowing the user to position the deposition head in the desired location within the enclosure before starting part fabrication. The movement to the corner of the enclosure during "homing" brings the deposition head to a position where there is not enough clearance between the side of the enclosure and the welder/frame assembly. This means that each time a part is run, the user must run the "homing" procedure prior to attaching the welder/frame assembly for part fabrication. This aspect of the part system became a key consideration during the next stage of hardware design, as discussed in the next section.

Mounting and Heat Delivery Hardware: Deposition Head to Substrate

The next stage of heat delivery is to transport the heated air from the welder, mounted on the side of the deposition head, to the substrate material. Since the deposition head can move in any direction, a fully functional PDHS should also be able to heat the substrate in any direction. However, for this work it was decided to restrict movement of the deposition nozzle to one axis—specifically the x-axis, which runs from left to right (from the front of the enclosure). This restriction was to simplify the heat

delivery requirements, as now the heated air only needs to be applied to the left and to the right of the material nozzle, rather than all the way around it.

The design of this section of hardware proved to be challenging, owing to the limited clearance available between the substrate material and the underside of the deposition head, approximately 0.011 m. The first design was to use one nozzle to direct the air in a flat stream pattern, heating the material on either side of and directly beneath the material nozzle. First, a stainless steel nozzle was connected to the copper tubing; however, the nozzle was too large to fit under the deposition head, and the distance from the edge of the deposition head to the material nozzle allowed for too much cooling of the air stream. For the next iteration, it was decided to shape the nozzle out of the tube itself in order to fit the required clearance.

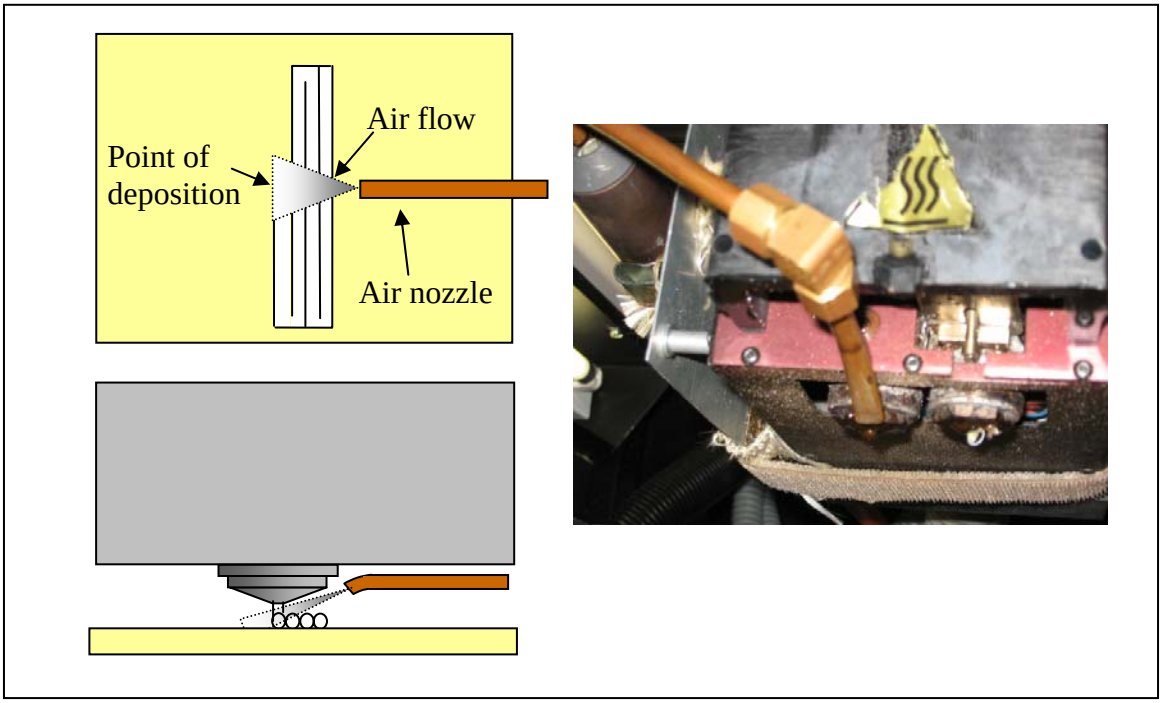

Figure 7. One-nozzle design for air delivery hardware.

The next design iteration used straight pieces of copper tubing with elbow fittings to bring the air into position in front of the nozzle, and a piece of copper tubing to bring the air as close to the nozzle as possible. This piece was flattened slightly for better clearance, and the end was shaped to direct the air in a flat spray, angled slightly downward (see Figure 7). A trial run of this system, however, produced parts with grossly inaccurate geometry (see

Figure 8). The cause of this was the air stream hitting the molten material as it was being extruded from the nozzle and blowing it out of the nozzle path.

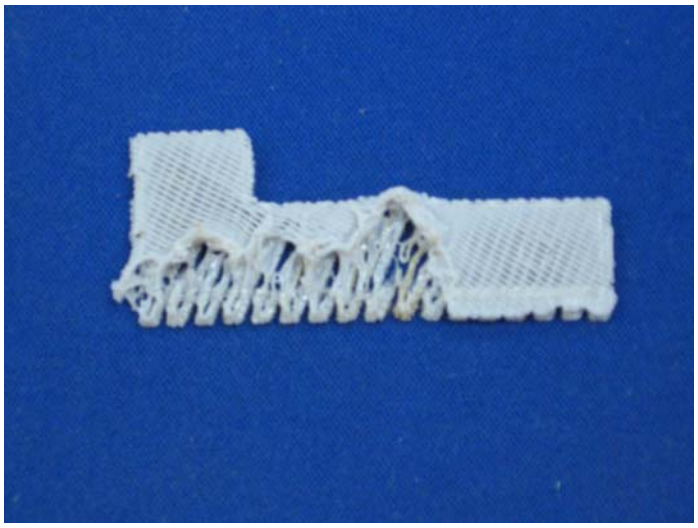

Figure 8. Aborted part made with one-nozzle design.

The negative impact of the air blowing directly at the FDM material nozzle resulted in a shift of design. Rather than using a single nozzle to deliver a wide stream of air, the next design used two nozzles to deliver the air to the substrate on either side of

the material nozzle. This design used a “tee” fitting to split the air at the base of the deposition head into two streams, each of which is crimped at the end and has a 0.254 cm diameter hole drilled directly in line with the material nozzle (see Figure 9).

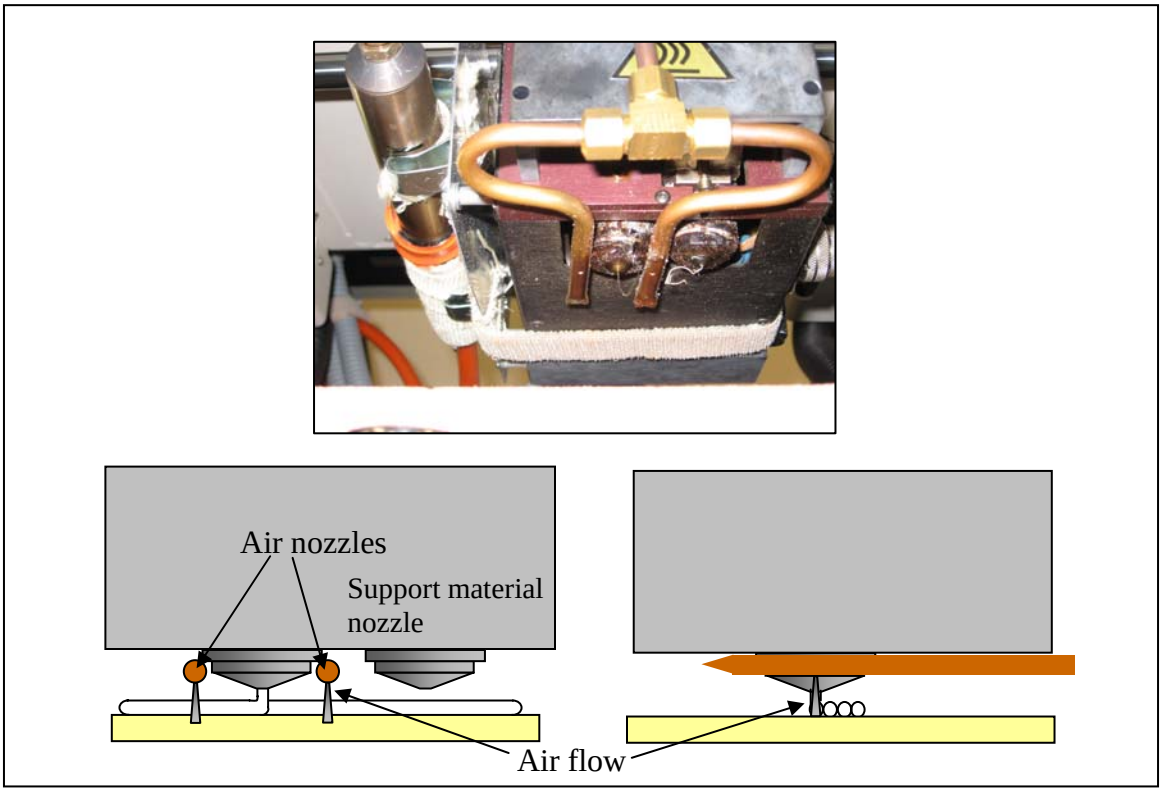

Figure 9. Two-nozzle design for air delivery hardware.

This design worked well in the first trial runs, and produced several good parts. However, in running these parts, the copper tubing was subjected to several heating-and-cooling cycles. Although the temperatures were not as high as those typically used to anneal copper, this repeated heating and cooling caused the copper tubing to soften to the point where the tubes running under the deposition head began to drag in the substrate material. In addition, the continual removal and re-attachment of the system (as described in the previous section) combined with the softening of the tubing made it

difficult to keep the air holes aligned properly with the FDM material nozzle. The loss of rigidity and alignment issues with the copper tubing fixture led to the next design iteration. In this design, a length of copper tubing connects the welder to a machined aluminum block, which is clamped onto a plastic component on the front of the deposition head. The block has been machined to channel the air into two 0.317 cm brass tubes, which deliver the air to the substrate in a similar manner as the previous design: each tube is crimped at the end and has a 0.127 cm diameter hole drilled in line with the deposition head. This design has several advantages over previous designs. The support from clamping the aluminum plate to the FDM deposition head provides much better support and rigidity than the previous systems, which relied on the stiffness of the copper tubing to maintain necessary clearances and positioning. In addition, clamping the aluminum block to the head allows for permanent placement of the air stream, since the welder/frame assembly can be easily attached or unattached by screwing or unscrewing the copper tubing fitting in the aluminum block (and the aluminum block does not have clearance issues during the "homing" procedure). This allows for much better consistency in keeping the air holes aligned with the model material nozzle than previous designs.

Once the system was in place, the placement of the air flow was adjusted. First, it was important to ensure that the air flows were properly aligned with the nozzle. Second, the air stream needed to be as close to the material nozzle as possible—but not to the point where the air disturbed material deposition. In order to determine where the air stream was hitting relative to the nozzle, a folded strip of paper with heat-sensitive ink

(used in a type of receipt printer for retail stores) was placed directly beneath the material nozzle. The heat of the nozzle and the heat from the air streams would mark the paper strips, allowing the position of the air flow relative to the nozzle to be determined (see Figure 10). Alignment issues were corrected by adjusting the length of the brass tubes, while the distance from the air to the nozzle was adjusted by rotating the tubes. After each adjustment, a part would be run to make sure that the air flows were not too close. In this way, it was determined that the closest the air stream could be without significantly affecting material flow was approximately 1.09 cm.

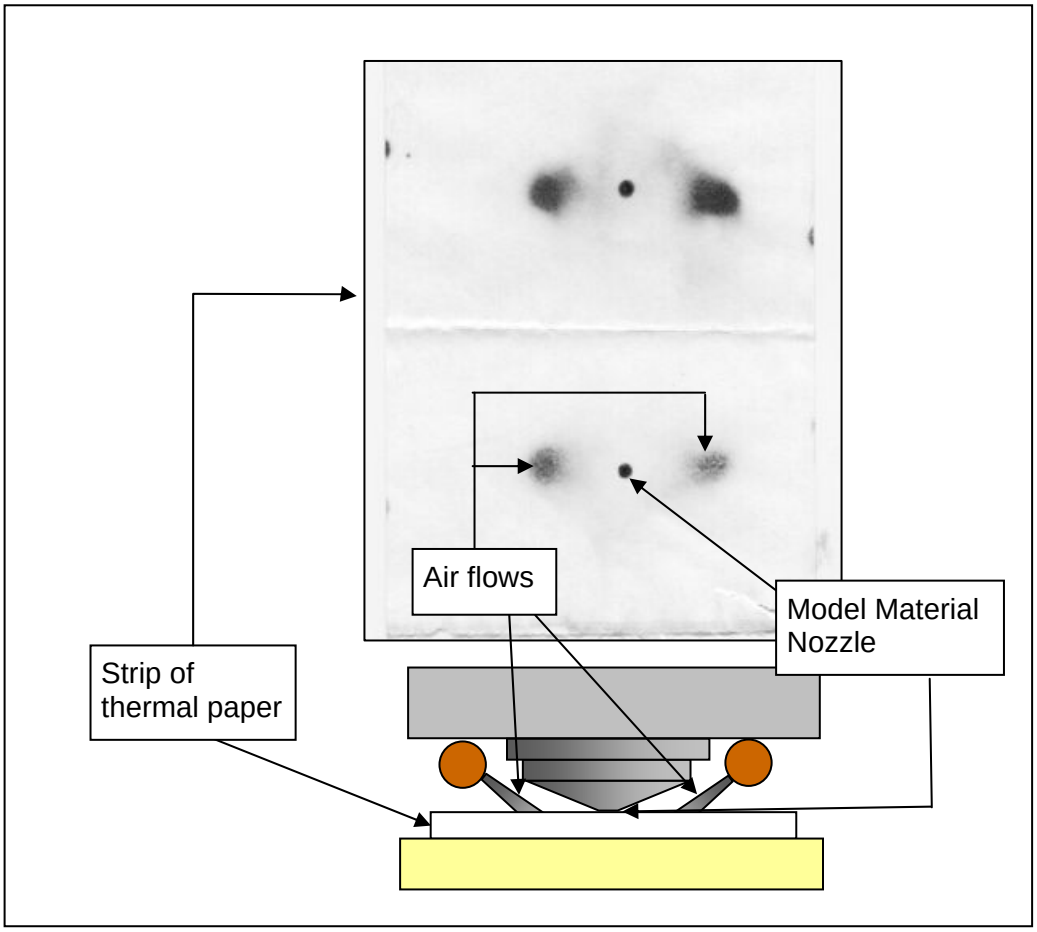

Figure 10. Strip of thermal paper used to check position of air flows.

The final component to making parts was determining where to set the envelope temperature. As mentioned in the introduction, this temperature is maintained by a heater and fan system, and the envelope temperature setting recommended by Stratasys for this material is 70^0 C. However, an issue with the temperature control system of the FDM made using the envelope temperature infeasible. In practice it is not uncommon for the machine to shut down if the door is left open too long when the envelope temperature is set to 70^0 C. The reason for this is that the open door causes the envelope temperature to drop, causing the heater to switch on to return the temperature to the specified setting; the heater causes the temperature to rise so fast that it continues rising, even after the specified temperature is reached and the fans turn on. This overcorrection does not usually cause a problem, unless it takes the envelope temperature above the maximum temperature allowed by the FDM machine, 75^0 C, in which case the machine automatically shuts off. During the development of the PDHS, it became apparent that additional heat put out by the PDHS was more than the fan controlling the envelope temperature could handle. As a result, it became necessary to prop the door open slightly in order for the FDM to maintain a somewhat constant envelope temperature. However, this and the additional air flow circulating in the FDM cause there to be a greater fluctuation in the envelope temperature than usual. With this amount of fluctuation in mind, the envelope temperature for PDHS parts was set to 65^0 C to avoid surpassing the maximum allowable temperature.

EXPERIMENTAL DESIGN

An experiment was needed in order to measure the effects of the pre-deposition heating system (PDHS) discussed in the previous chapter. This chapter discusses the design and procedures of this experiment, beginning with the design of the test part used to measure the variables of interest, followed by a brief discussion of the statistical principles used to analyze the experimental data. The chapter ends with the development of the experimental design used in this work.

Test Part Design

As described in the Introduction, the goal of the PDHS is to improve part interlayer strength without negatively impacting the material properties or dimensional accuracy. Therefore, the test part used to in the experiment was designed to allow for measurements of interlayer strength, road tensile strength (to test for material degradation), and dimensional accuracy. The test part design is shown in Figure 11.

The vertical section of the part provides data for interlayer strength and dimensional accuracy. As the major concern regarding dimensional accuracy is that the part may slump due to the additional heating (damaging the dimensional accuracy in the vertical direction), the height of the vertical section will be measured in each part to detect any changes in dimensional accuracy. Three measurements will be taken from the vertical section: 0.635 cm from either side and in the middle. The average height will be

compared with the nominal height of 6.35 cm, and the percent deviation will be used in the analysis.

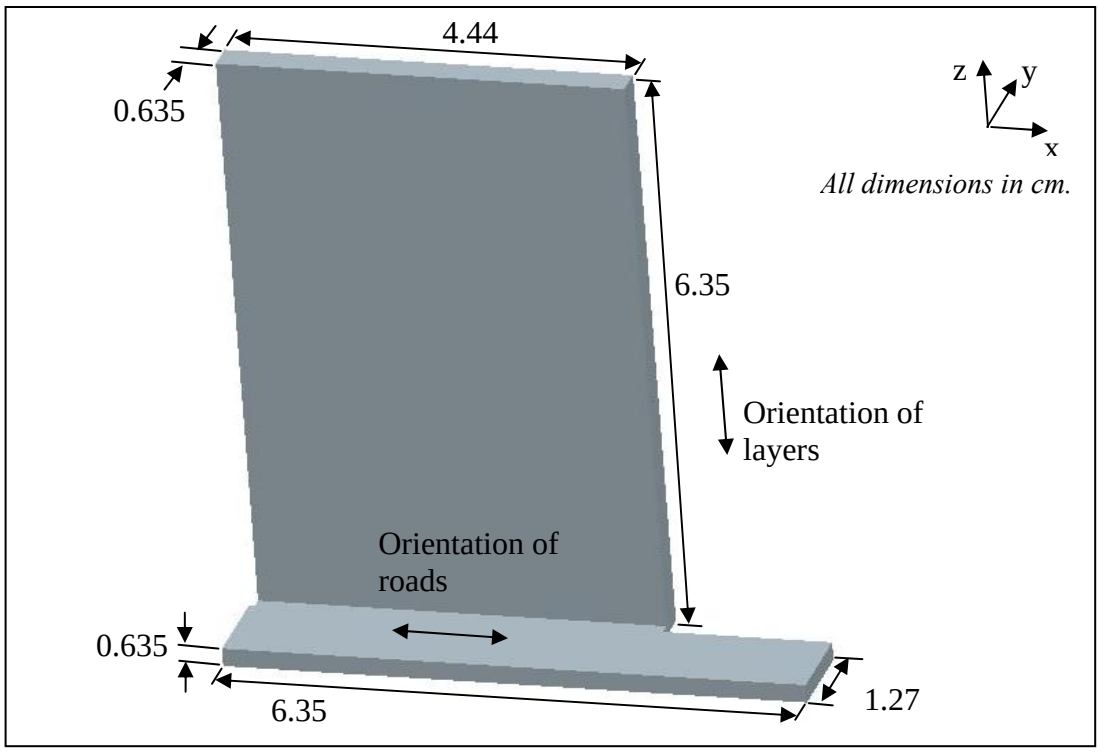

Figure 11. CAD model of the test part.

After the necessary measurements have been taken, the vertical section of the part will then be machined into a tensile test specimen, using the test specimen geometry prescribed by ASTM for plastic specimens [46]. Defects in FDM usually occur at the ends of roads, when the nozzle has to change direction. A change in nozzle direction causes a change in deposition speed, where which can cause errors in the coordination between the deposition head drive system and material rollers, leading to surface and internal defects [17]. Thus, machining the specimen out of the center of the vertical section was a measure to reduce the risk of defective test samples.

The flat section of the part was designed to measure the axial strength of the part. The roads for this section were specified in QuickSlice© to run along the length of the part, so that a test specimen from this section would test the strength of the roads themselves. The purpose of this test was to check for degradation of material properties due to overheating of the material.

Analysis of Variance (ANOVA)

Analysis of Variance (ANOVA) is the term given to a type of statistical analysis used to detect changes of some response variable in a group of samples, usually due to user-controlled changes in one or more sample treatments. The foundation of ANOVA is statistical hypothesis testing, where a null hypothesis is tested against an alternate hypothesis based on a level of significance. In ANOVA, the null hypothesis is that the means of all of the sample groups—that is, groups of sample produced at each level of each treatment—are the same. The comparison between groups is made by splitting the total sum of square, a measure of deviation from the overall mean, into two components: deviation due to the treatment differences, and deviation due to error or variation within a sample group. The sums of squares due to these potential sources of variation are converted into mean squares, which allows for a test for statistical significance using Fisher's F-distribution, based on a user-selected level of significance [47].

The results obtained using ANOVA are usually summarized in an ANOVA table, as shown below in

Table 1.

Table 1. ANOVA table for one-way classification.

Source of variation	*Degrees of freedom*	*Sum of Squares*	*Mean Square*	*F*
Treatments	*k-1*	*SS(Tr)*	*MS(Tr) = SS(Tr)/(k-1)*	*MS(Tr)/MSE*
Error	*N-k*	*SSE*	*MSE = SSE/(N-k)*	
Total	*N-1*	*SST*		

Where:

$$SST = \sum_{i=1}^{k}\sum_{j=1}^{n_i} y_{ij}^2 - C \tag{5}$$

$$SS(Tr) = \sum_{i=1}^{k} \frac{T_i^2}{n_i} - C \tag{6}$$

$$SSE = SST - SS(Tr) \tag{7}$$

$$C = \text{Correction term} = C = \frac{T_\bullet^2}{N} \tag{8}$$

$$T_i = \sum_{j=1}^{n_i} y_{ij} \tag{9}$$

$$T_\bullet = \sum_{i=1}^{k} T_i \tag{10}$$

$$N = \sum_{i=1}^{k} n_i \tag{11}$$

with i= number of treatments, n_i = sample size of treatment i, and y_{ij} = jth observation of the ith treament.

In ANOVA analysis, the “degrees of freedom” refers to the number of observations that can contribute to the analysis. A general rule of thumb to ensure adequate statistical resolution is to have at least 10 degrees of freedom for experimental error [48]. This requirement can be satisfied by adjusting the number of observations taken.

The ANOVA analysis can be extended from one factor, as described above, to many factors. An experiment where the treatments are combinations of two or more factors is known a factorial experiment. The analysis for a two-factor experiment is essentially an extension of ANOVA analysis to two treatments, with one major distinction: the treatment sum of squares is usually divided into three components, one for each treatment, one for the interaction—or joint effect—of the two treatments, and one for the effect of the replication. The table below illustrates the ANOVA table for a two-factor experiment for treatments A and B.

Table 2. ANOVA table for two-factor experiment

Source of Variation	*Degrees of freedom*	*Sum of squares*	*Mean square*	*F*
Main Effects:				
A	a-1	*SSA*	*MSA*	*MSA/MSE*
B	b-1	*SSB*	*MSB*	*MSB/MSE*
Interaction	(a-1)(b-1)	*SS(AB)*	*MSI*	*MSI/MSE*
Replication	r-1	*SSR*	*MSR*	*MSR/MSE*
Error	(ab-1)(r-1)	*SSE*	*MSE*	
Total	abr-1	*SST*		

Where:

$$SSA = \frac{1}{b \cdot r} \sum_{i=1}^{a} \left(\sum_{j=1}^{b} \sum_{k=1}^{r} y_{ijk} \right)^2 - C \qquad (12)$$

$$SSB = \frac{1}{a \cdot r} \sum_{j=1}^{b} \left(\sum_{i=1}^{a} \sum_{k=1}^{r} y_{ijk} \right)^2 - C \qquad (13)$$

$$SS(AB) = SS(Tr)\text{-}SSA\text{-}SSB \qquad (14)$$

$$SS(Tr) = \frac{\sum_{i=1}^{a}\sum_{j=1}^{b}\left(\sum_{k=1}^{r} y_{ijk}\right)^2}{r} \quad (15)$$

$$SSR = \frac{\sum_{k=1}^{r}\left(\sum_{i=1}^{a}\sum_{j=1}^{b} y_{ijk}\right)^2}{ab} \quad (16)$$

$$SSE = SST\text{-}SS(Tr)\text{-}SSR \quad (17)$$

$$SST = \sum_{i=1}^{a}\sum_{j=1}^{b}\sum_{k=1}^{r} y_{ijk}^2 - C \quad (18)$$

$$C = \frac{\left(\sum_{i=1}^{a}\sum_{j=1}^{b}\sum_{k=1}^{r} y_{ijk}\right)^2}{abr} \quad (19)$$

with a = number of levels of A, b = number of levels of B, and r = number of replications.

The ANOVA analysis detects whether the treatment effects account for a significant difference in the response variable. However, it is usually useful to quantify the amount of difference in some way. One method of doing this is the Duncan multiple-range test, which compares the range of a set of p means to a variable known as the least significant range, R_p, defined by:

$$R_p = s_{\bar{y}} \cdot r_p \quad (20)$$

Where

$$s_y = \sqrt{\frac{MSE}{n}} \quad (21)$$

and r_p is the critical value for the number of means, p, associated with the chosen level of significance and the number of degrees of freedom corresponding to *MSE*. Values for r_p have been tabulated and are available in many statistics handbooks; the values in this work are from Miller and Freund [49]. The procedure for using the Duncan multiple-range test is to order the sample means, calculate the ranges for a given value of p, and compare those ranges with the values of R_p. A range of sample means that is greater than its corresponding value of R_p indicates a significant difference between the means. The results from the Duncan multiple-range test are usually displayed as shown below in Figure 12. Lines are drawn under adjacent means for which the differences are not significant.

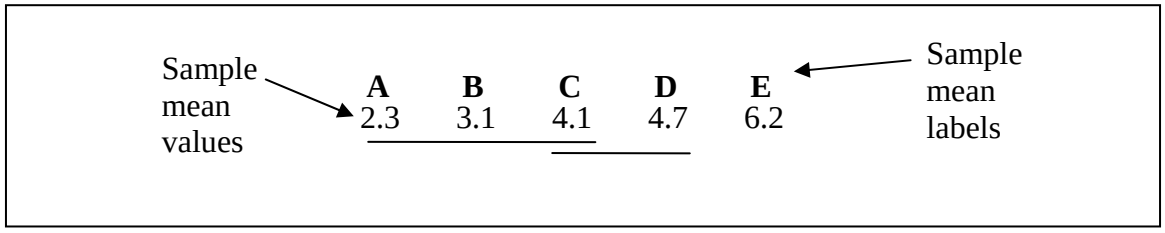

Figure 12. Results diagram for Duncan multiple-range test

Experimental Design

To analyze the effects of the PDHS, an experiment was designed using the test part design and statistical principles discussed above. The experiment has two components: a one-factor experiment examining the effects of the PDHS compared to normal FDM, and a two-factor experiment, using a subset of the data from the first analysis, examining the effects of voltage (controlling temperature) and air flow in parts

made using the PDHS. The "treatment" of the one-factor analysis is the environmental heating method (non-PDHS vs. PDHS) at several different levels, including parts made at different voltages and air flow levels with the PDHS. The data from the parts made using the PDHS will then be examined using a two-factor analysis to investigate the effects of the PDHS temperature and air flow. The first step in the experimental design was to select the treatment levels of each factor.

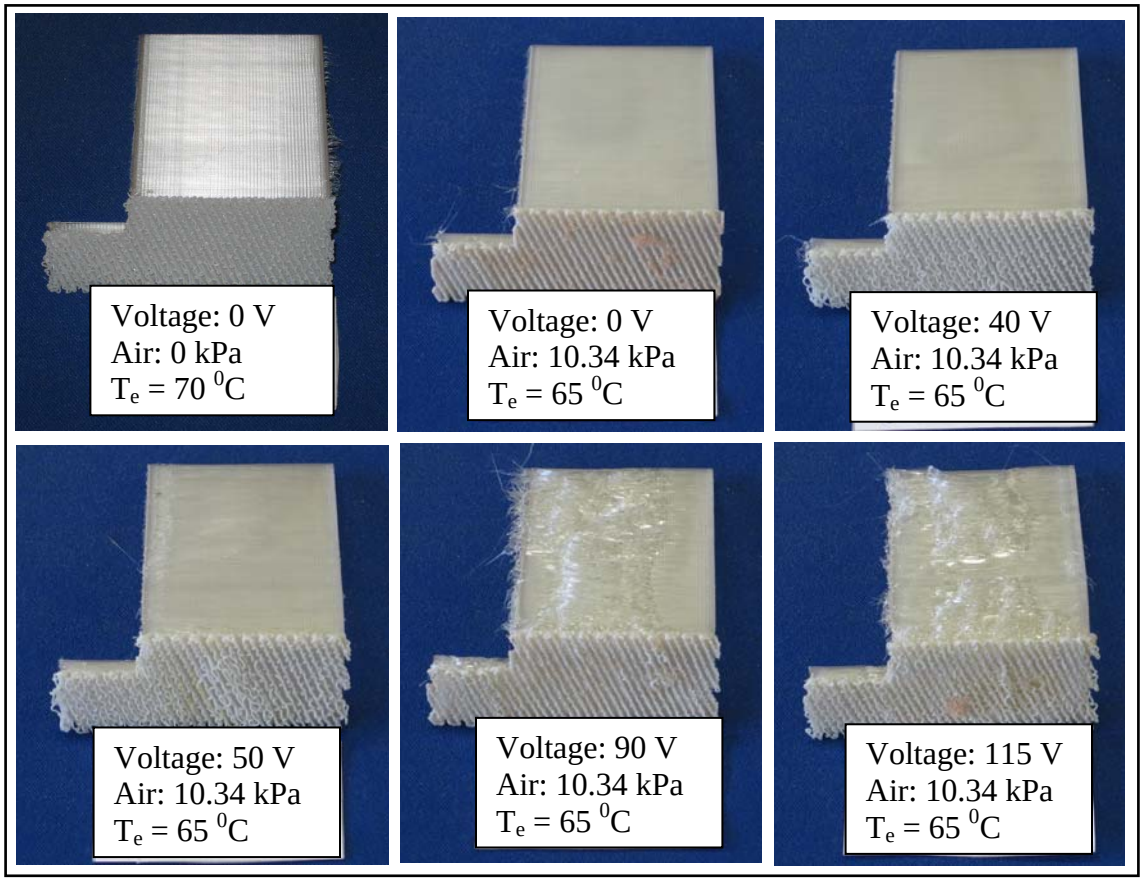

Figure 13. Test parts created to aid in the selection of PDHS treatment levels.

To aid in the selection of levels of PDHS voltage and air flow, a set of parts were made at a range of voltages: 0V, 40V, 50V, 90V, and 115V. The air pressure setting for

these samples was set at 10.34 kPa (1.5 psi), which was the lowest pressure that the flow switch was able to maintain. As discussed in the previous chapter, the envelope temperature was set to 65^0 C. Images of these samples are shown below in Figure 13. The images show how the surface finish degrades as the temperature of the PDHS increases. Parts made at 50 V and higher showed increasingly severe waviness of the roads on the side surfaces of the upright section of the test part. Parts made at 40 V or below showed little or no waviness of the surface layer. This waviness of the surface layer of roads appears to be due to a combination of heat and air flow, at higher temperatures, the material stays softer and is more easily disturbed by the air flow.

The roads on the surface are the first roads to be deposited on each layer, so they are especially prone to this disturbance, as they are only supported from the bottom—where internal roads are supported from the bottom and from the side of the previous road. While this loss in geometric accuracy is not desirable, it was decided to include the higher temperatures in the experiment to see if there was an increase in interlayer strength.

Another note of interest is that during fabrication of the parts at the highest voltage (115 V), the PVC welder overheated and had to be replaced. To avoid this in the experiment, it was decided to set the maximum voltage setting of the PVC welder to 90 V. Based on this consideration and the pilot study, four voltage levels were selected for the experiment: 0 V (air only), 40 V, 65 V, and 90 V. To examine how the amount of air flow affected the process, two levels were chosen for the air pressure: 10.34 kPa and

20.68 kPa. These values of PDHS voltage and air pressure comprise the levels of the two-factor experiment, making it a 4 x 2 factorial experiment.

The goal of the one-factor analysis was to compare parts fabricated using the PDHS with those made without it. Therefore, it was necessary that at least one level of treatment would be parts made without the PDHS. Without the PDHS, the remaining environmental parameter is the envelope temperature. Two levels were selected for non-PDHS parts: one level with an envelope temperature of 70^0 C and one level at an envelope temperature at 65^0 C. The level at 65^0 C was chosen to match the envelope temperature selected for the PDHS parts, which allows for comparison between parts made with and without the PDHS with all other parameters being the same.

In summary, the one-factor experiment was designed with 10 levels of treatment, and the two-factor study was designed as a 4 x 2 factorial experiment (4 levels of the voltage treatment, 2 levels of the air flow treatment). This information is summarized in Table 3. Throughout the rest of this report, samples will be identified as they are in the table, with a three-number label. The first number refers to the voltage setting of the PDHS, the second number indicates the air pressure setting (in kPa), and the third number indicates the envelope temperature (in degrees C). For example, the samples made without the PDHS at 65^0 C will be labeled “0/0/65”.

Table 3. Description of the experiment treatment levels

Analysis	*Treatment*	*Levels*
One-factor experiment	*Environmental Heating* __V/___kPa/___^{0}C	1. 0/0/65 2. 0/0/70 3. 0/10.34/65 4. 0/20.68/65 5. 40/10.34/65 6. 40/20.68/65 7. 65/10.34/65 8. 65/20.68/65 9. 90/10.34/65 10. 90/20.68/65
Two-factor experiment	*PDHS Voltage*	1. 0V 2. 40V 3. 65V 4. 90V
	PDHS Air pressure	1. 10.34 kPa 2. 20.68 kPa

The next component of experimental design was to set the sample size. As mentioned in the ANOVA background section, a general rule of thumb is to set the sample size for each treatment so that the error degrees of freedom are greater than 10. With this rule of thumb in mind, the sample size was set at five samples per treatment level, or five replications (where one replication is one sample of each treatment). This gives 40 error degrees of freedom for the one-factor analysis and 28 error degrees of freedom for the two-factor analysis. In addition to satisfying the requirements for error degrees of freedom this sample size is in line with most ASTM standards, which specify a minimum sample size of five [46].

PDHS Characterization for Temperature and Air Speed

As discussed previously, the welder used in the PDHS is not currently capable of maintaining a constant temperature. As a result, the welder voltage is used as the parameter that controls temperature, with the understanding that each voltage corresponds to a range of temperatures. Before the experiment was conducted, the welder was run for over 90 minutes (the anticipated run time of the test parts) at the three PDHS voltages selected for the experiment, with a thermocouple monitoring the air temperature at the nozzle. The results of this test are displayed in Figure 14, with the minimum, maximum, average, and range of temperatures corresponding to each voltage given in Table 4.

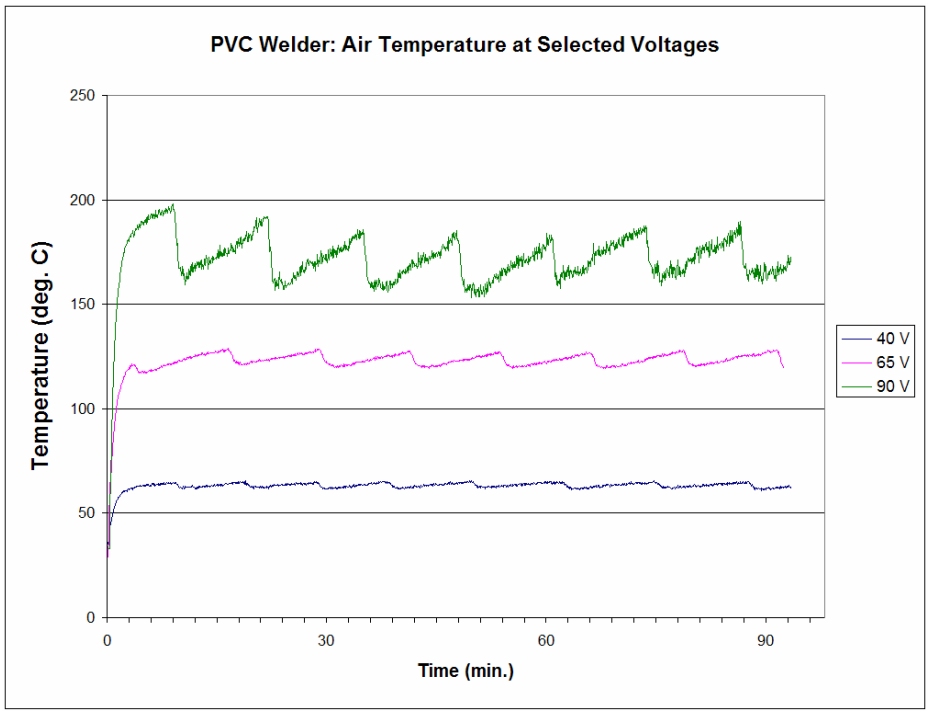

Figure 14. Exit air temperatures at PDHS experiment voltages.

Table 4. Temperature statistics for PDHS experiment voltages (excluding 10 min. warm-up)

PDHS Voltage:	*40 V*	*65 V*	*90 V*
Minimum Temp. (^{0}C)	60.83	119.16	153.16
Maximum Temp. (^{0}C)	65.61	129.0	197.88
Average Temp. (^{0}C)	63.27	123.66	170.61
Temperature Range (^{0}C)	4.78	9.84	44.72

The results from the temperature characterization show that the range of temperatures increases dramatically with the voltage. The amount of fluctuation in the 90V case is especially disappointing; however, since this work is a proof of concept and the range of temperatures corresponding to each of the voltages do not overlap, this variation was deemed acceptable for the experiment.

The exit air flow rate of the PDHS was calculated using the continuity equation and Bernoulli's equation [50]. The flow rates for each voltage are given in Table 5, and the analysis is contained in Appendix C.

Table 5. Exit air flow rates

Pressure (kPa)	Flow Rate (m^3/s)
10.34	5.72×10^{-5}
20.68	8.03×10^{-5}

Fabrication & Test Procedure

Test parts were modeled using Pro-Engineer Wildfire© software, and fabricated using a Stratasys FDM 1650 from P500 MABS feedstock material. This material is the medical grade of ABS plastic produced by Stratasys Corporation. In keeping with statistical principles, the order of production was randomized within replications using the random number generator in Microsoft Excel©. With the exception of the envelope

temperature, the FDM processing parameters were set as recommended by Stratasys Corporation for this material (see Appendix A).

Following deposition, the support material base was removed and the vertical section of the sample part was measured in three locations to provide data for the dimensional accuracy of the part. Following the basic procedure used by Grimm [15], dimensional accuracy was quantified by measuring the height of the vertical section three places (.635 cm from each end and in the center) and calculating the percent deviation of the average of these heights from the nominal value (6.35 cm). The reason the vertical dimension was selected for this data was that dimensional errors would additively cause deviation from the nominal dimension—in other words, the vertical dimension captures the entire deposition history.

Once the dimensional data is taken, the vertical and flat sections of the test part were separated by hand, and prepped for machining by lightly running a file over the surfaces to provide a level surface for proper seating in the fixture.

Test specimens were machined using a Haas CNC Mill. Coolant was used to minimize the risk of damaging the parts, which meant that the test specimens were somewhat damp after machining. They were dried off manually using paper towels, and then placed in the FDM enclosure (with the envelope temperature at 65^0 C) for twenty-four hours as a way of removing excess moisture. It is worth noting that the main focus of the experiment was comparing the data between samples rather than finding definitive values (e.g. for a properties database), and so having samples that were completely dry was not necessary. All samples were machined, stored, and tested together, so it is

unlikely that differences in part strength could be attributed to variability in processing, temperature, or humidity (moisture).

Tensile tests were performed using a model 3343 Instron machine, at a rate of 1 cm/min. Prior to testing, the cross-sectional area and gage length of each specimen was measured, and used to calculate engineering stress and strain of the sample. This method of calculating stress treats the part as a homogenous material, and does not reflect the actual stress on the ABS material itself. This assumption and method is the same as the procedure used by Han *et al.* and Bellini *et al* to calculate strength in FDM parts [34,27].

RESULTS AND ANALYSIS

The experiment designed in the previous chapter called for the fabrication of 50 test parts, 5 parts for each level of environmental heating. However, parts could not be physically fabricated at the PDHS setting at 90V and 20.68 kPa (the highest level of temperature with the highest level of air flow) due to disruption of the material in deposition. An image of an attempted part at this setting is shown below in Figure 15, along with a successful part.

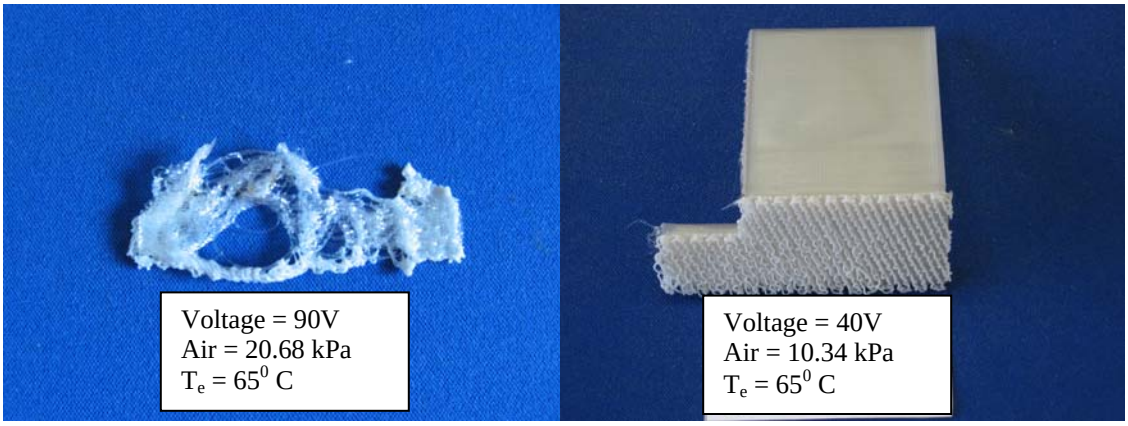

Figure 15. Parts created at different PDHS settings.

While this is an important result in this investigation, samples made at this level cannot contribute to the quantitative analysis. As a result, the number of samples actually fabricated and used in the analysis was 45. This number of sample results in 36 error degrees of freedom for the one-factor analysis, and 20 error degrees of freedom for the two-factor analysis, satisfying the accepted level for meaningful statistical sensitivity.

Dimensional Accuracy

The dimensional accuracy data for the 45 samples are shown in Figure 16. The figure shows the minimum, average, and maximum value for percent deviation in each sample group. The chart shows that samples fabricated using higher temperatures of the PDHS seem to have greater deviations from the nominal dimension, indicating a loss of dimensional accuracy.

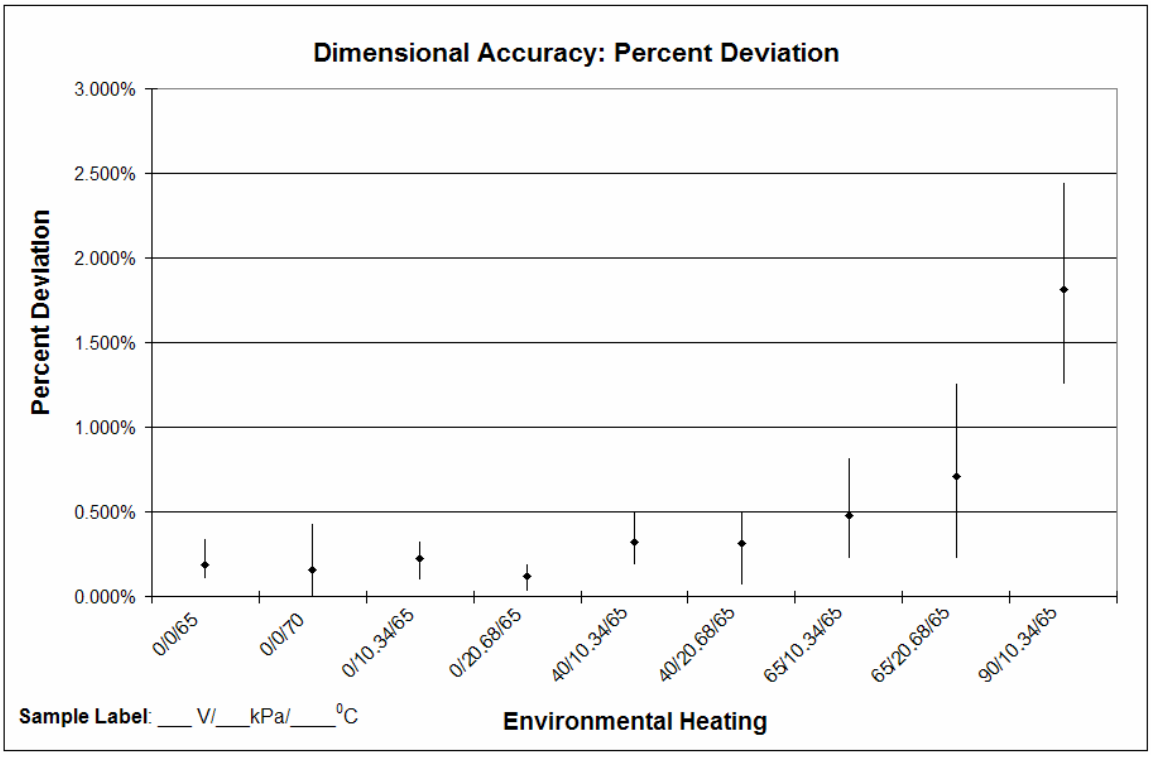

Figure 16. Dimensional accuracy of FDM parts

The ANOVA table for the one-factor analysis is shown below in Table 6. The Duncan multiple range test diagram for dimensional accuracy is shown in Figure 17.

Table 6. ANOVA table for one-factor analysis of dimensional accuracy.

ANOVA (Level of significance: α=5%)

Source of Variation	*deg. of freedom*	*SS*	*MS*	*F*	*P-value*	*F crit*	
Env. Heating	8	0.00076	1E-04	14.0617	8.9348E-09	2.22534	*
Error	34	0.00023	7E-06				
Total	42	0.00099					

* - Significant

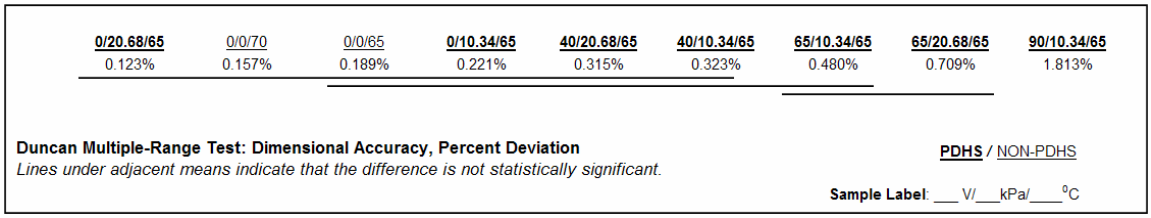

Figure 17. Duncan multiple-range test diagram for dimensional accuracy (one-factor experiment).

In the ANOVA table, F is greater than F_{crit}. This indicates that the null hypothesis of the analysis, that dimensional accuracy is the same for all sample groups, should be rejected (with a .05 probability of a Type I error)—that is, there is some statistically significant variation of the dimensional accuracy. The Duncan multiple-range test indicates that the samples made without the PDHS and samples made with low PDHS voltages had significantly better dimensional accuracy than samples made with higher voltages. In particular, the samples made at the highest temperature had the worst dimensional accuracy. The ANOVA table for the two-factor analysis is shown in

Table 7. With the removal of the 90V/20.68/65^{0}C specimens, the analysis changes from a 4x2 factorial experiment to a 3x2 factorial experiment, with three levels of voltage instead of four.

Table 7. ANOVA table for two-factor analysis of dimensional accuracy.

ANOVA (Level of significance: α=5%)

Source of Variation	*Degrees of freedom*	*Sum of Squares*	*Mean Square*	*F*	*$F_{critical}$*	
Replication	*4*	*0.0001*	*1.28E-05*	*1.2223245*	*2.87*	
Main Effects:						
Voltage	*3*	*0.0001*	*3.07E-05*	*9.1305599*	*3.49*	** - Significant*
Air press.	*1*	*0.0000*	*1.25E-06*	*0.3728869*	*4.35*	
Interaction	*3*	*0.0000*	*4.78E-06*	*1.421881*	*3.49*	
Error	*28*	*0.0001*	*3.36E-06*			
Total	*39*	*0.0003*				

The table indicates that only the voltage setting significantly affects the dimensional accuracy. Applying the Duncan multiple-range test to the different voltage sample groups shows that the highest voltage (60V, in this analysis) has an average percent deviation that is significantly higher than the other two voltage settings (0V, 40V), as shown in Figure 18.

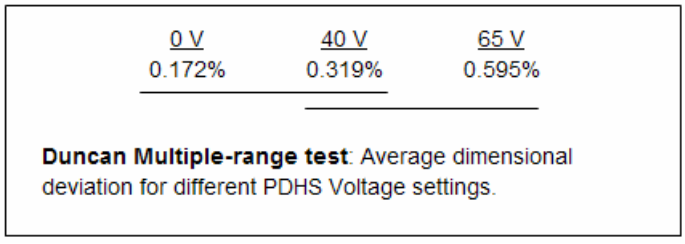

Figure 18. Duncan multiple-range test diagram for dimensional accuracy (2 factor experiment).

Material Properties

The initial procedure for testing for deviation in material properties was to machine axially-oriented tensile test specimens out of the horizontal portion of the test part. However, the orientation of the roads made machining these specimens extremely difficult. The edge of the cutting tool would invariably catch one of roads and cause a massive delamination (see Figure 19).

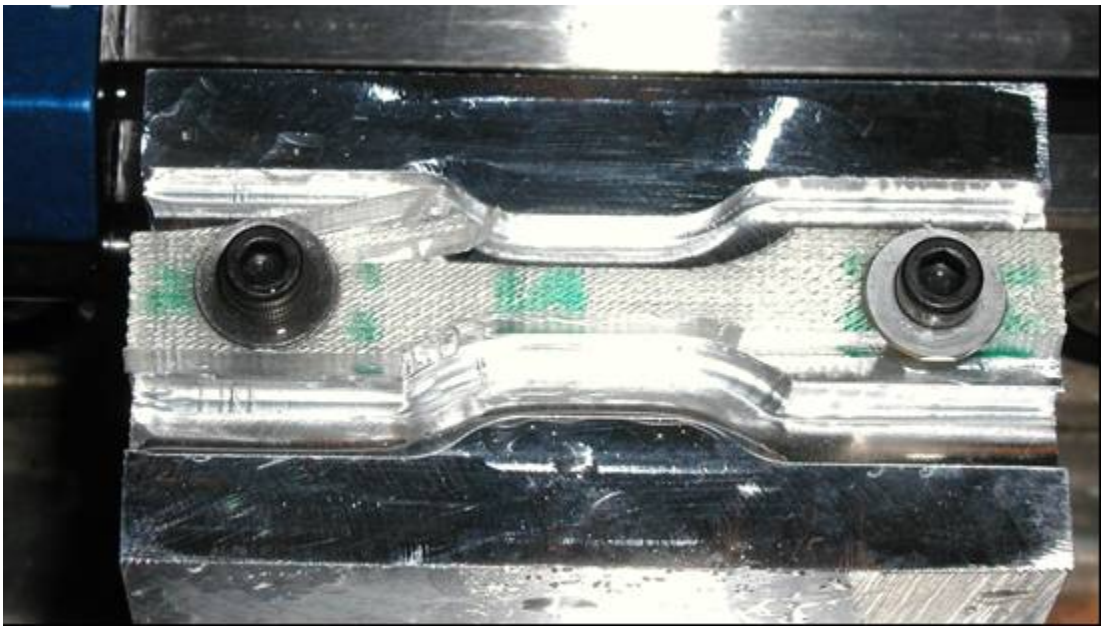

Figure 19. Delaminated tensile test specimen in the axial direction.

It was then reasoned that since loads were only carried by the roads that ran the length of the test specimen (i.e. roads that were in the narrow section of the "dog bone" geometry), straight tensile test specimens would be a logical substitution for the "dog bones". A set of straight samples were fabricated, and PVC tabs were glued onto the grip sections using epoxy, in an attempt to prevent grip failures from occurring. Despite this precaution, all samples failed in the grips. The next attempt was to model and fabricate

the “dog bone” test specimen geometry directly, bypassing the machining step, and tabbing the grip sections. These specimens also failed at the grips.

As a result of the difficulties encountered with tensile testing in the axial direction, it was decided to test axially-oriented samples in three-point bending. Following the geometry specified by the ASTM standard for flexure tests for plastics, a set of axial samples (five samples per treatment level) were fabricated, with the roads running parallel to the length of the test specimen [51]. In addition, a set of three transverse samples were fabricated for each treatment level, with the roads running perpendicular to the length of the specimen (see Figure 20).

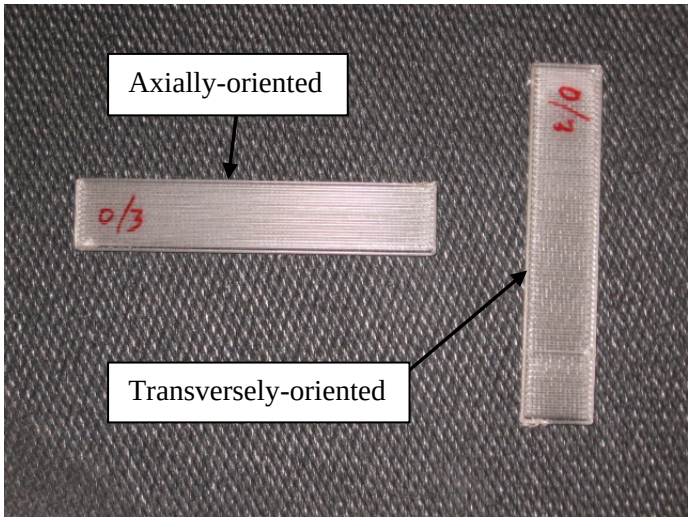

Figure 20. Flexure test specimens, oriented in the a.) axial and b.) transverse directions.

Flexure test specimens were tested in three-point bending on a model 3343 Instron testing machine, at a rate of 0.087 cm/min (see Figure 21).

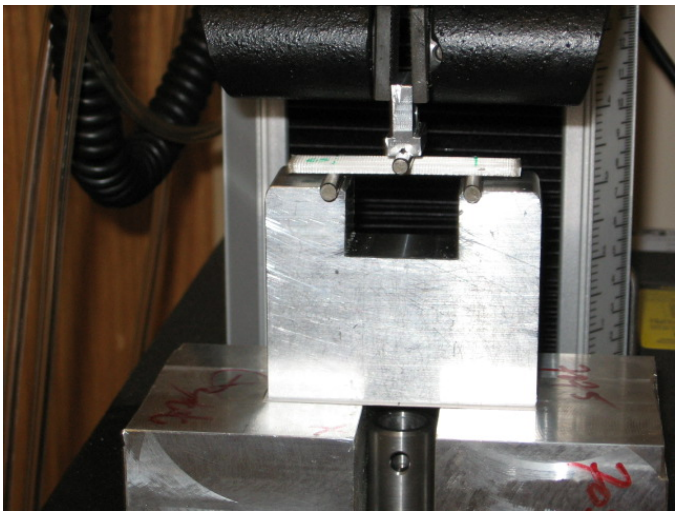

Figure 21. Flexure test specimen setup in three-point bending.

The force-displacement curves for an axial and transverse flexure sample fabricated at 40V/10.34kPa/65^{0}C are shown below. These curves are characteristic of all samples.

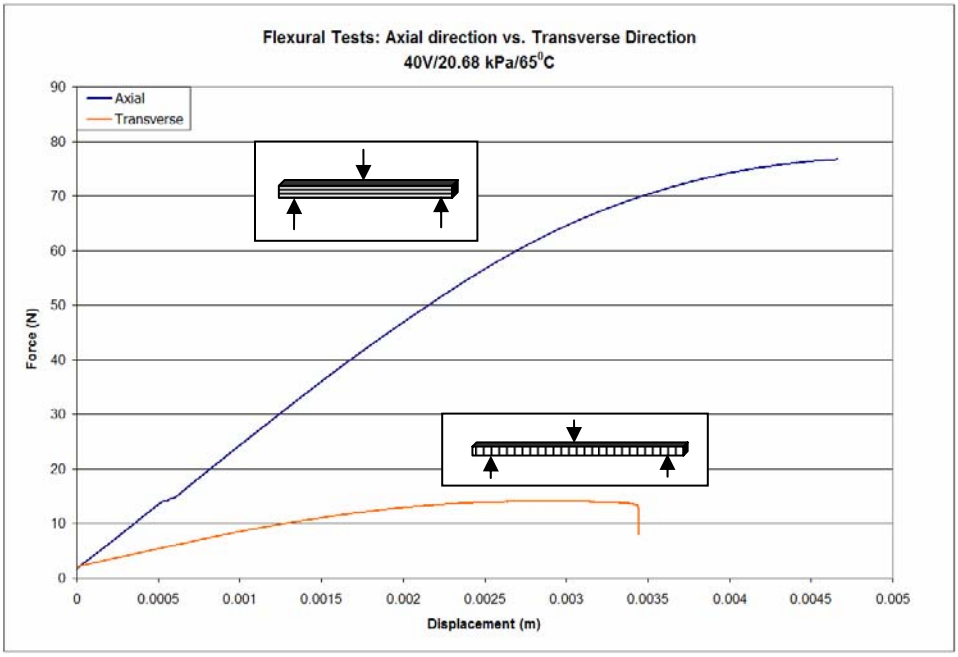

Figure 22. Force-displacement curves for axial and transverse specimens fabricated at 40V/20.68 kPa/65^{0}C.

The curves in Figure 22 show that there is a marked difference in both strength and stiffness in the two directions, which indicates a different failure mode. The results from the tests are shown in Figure 23 and Figure 24. The published flexural strength for this material is 58.6 MPa (see Appendix A).

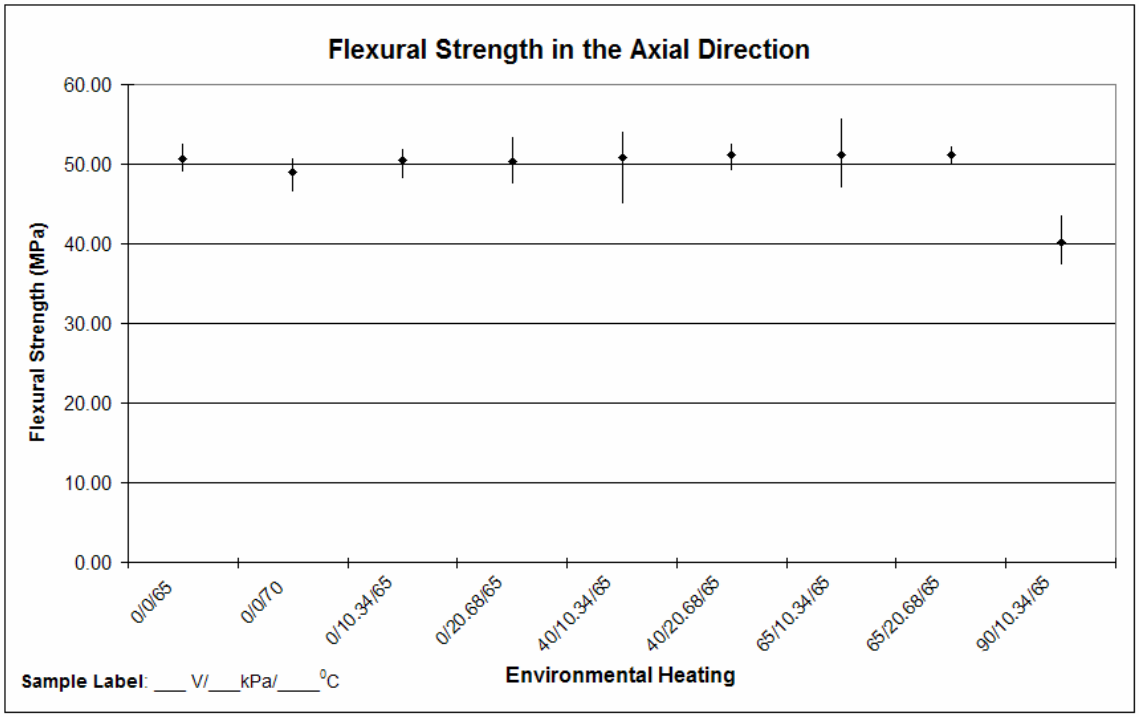

Figure 23. Flexure test results for specimens oriented in the axial direction.

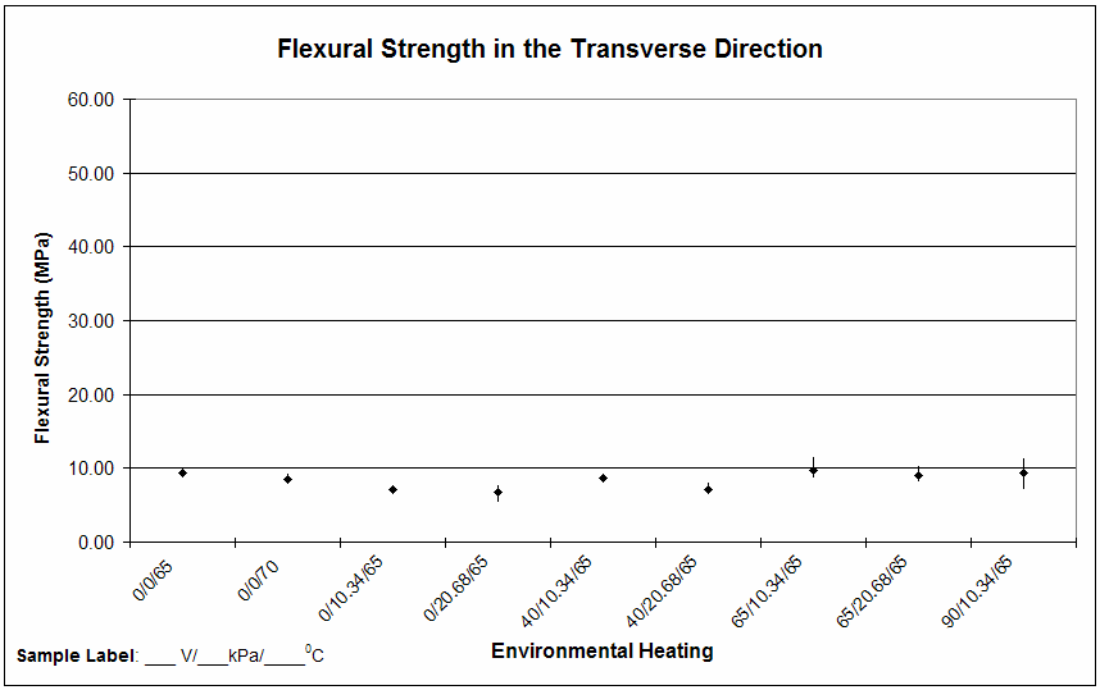

Figure 24. Flexure test results for specimens oriented in the transverse direction.

The magnitude of the difference between the strengths in the axial and transverse directions supports the use of the flexural data for the axial specimens to determine if the PDHS affects the strength of the material. The ANOVA table for the one-factor analysis is shown below in
Table 8, followed by the Duncan multiple-range test diagram in Figure 25.

Table 8. ANOVA table for one-factor analysis of flexural strength in the axial direction.

ANOVA (Level of significance: α=5%)

Source of Variation	*SS*	*df*	*MS*	*F*	*P-value*	*F crit*	
Env. Heating	507.8048	8	63.4756	12.5633	2.14E-08	2.2085181	*
Error	181.88917	36	5.05248				
Total	689.69397	44					

* - Significant

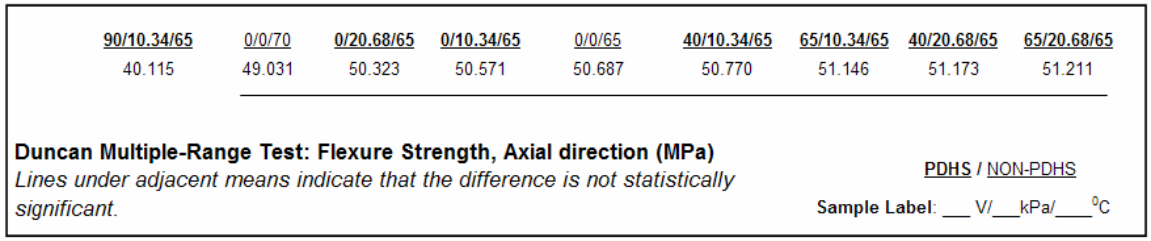

Figure 25. Duncan multiple-range test for the one-factor analysis of flexural strength in the axial direction.

As the values in the ANOVA table and Duncan test diagram show, samples made at 90V/10.34 kPa/65^{0}C show a significant reduction in flexural strength (with a .05 probability of committing a Type I error). This suggests that these samples experienced a loss of material properties, probably due to excessive heating or reheating.

The results of the one-factor analysis show that only samples produce at the 90V level show a significantly different flexural strength. Thus, the two-factor analysis, which only includes data from the lower three voltages (0V, 40V, and 65V), does not show any statistical difference between treatment levels (see Table 9).

Table 9. ANOVA table for two-factor analysis of flexural strength in the axial direction.

ANOVA (Level of significance: a=5%)

Source of Variation	*Degrees of freedom*	*Sum of Squares*	*Mean Square*	*F*	$F_{critical}$
Replication	*4*	*5.0452*	*1.2613*	*0.2754*	*2.87*
Main Effects:					
Voltage	*3*	*2.8437*	*0.9479*	*0.207*	*3.49*
Air press.	*1*	*0.0401*	*0.0401*	*0.0087*	*4.35*
Interaction	*3*	*0.5317*	*0.1772*	*0.0387*	*3.49*
Error	*28*	*128.2*	*4.5798*		
Total	*39*	*136.7*			

Interlayer Part Strength

Tensile tests were conducted for all 45 test parts. A group of the force-displacement curves are shown below in Figure 26. All samples failed in the narrow section of the test specimen, in a brittle fashion (no visible necking of the material).

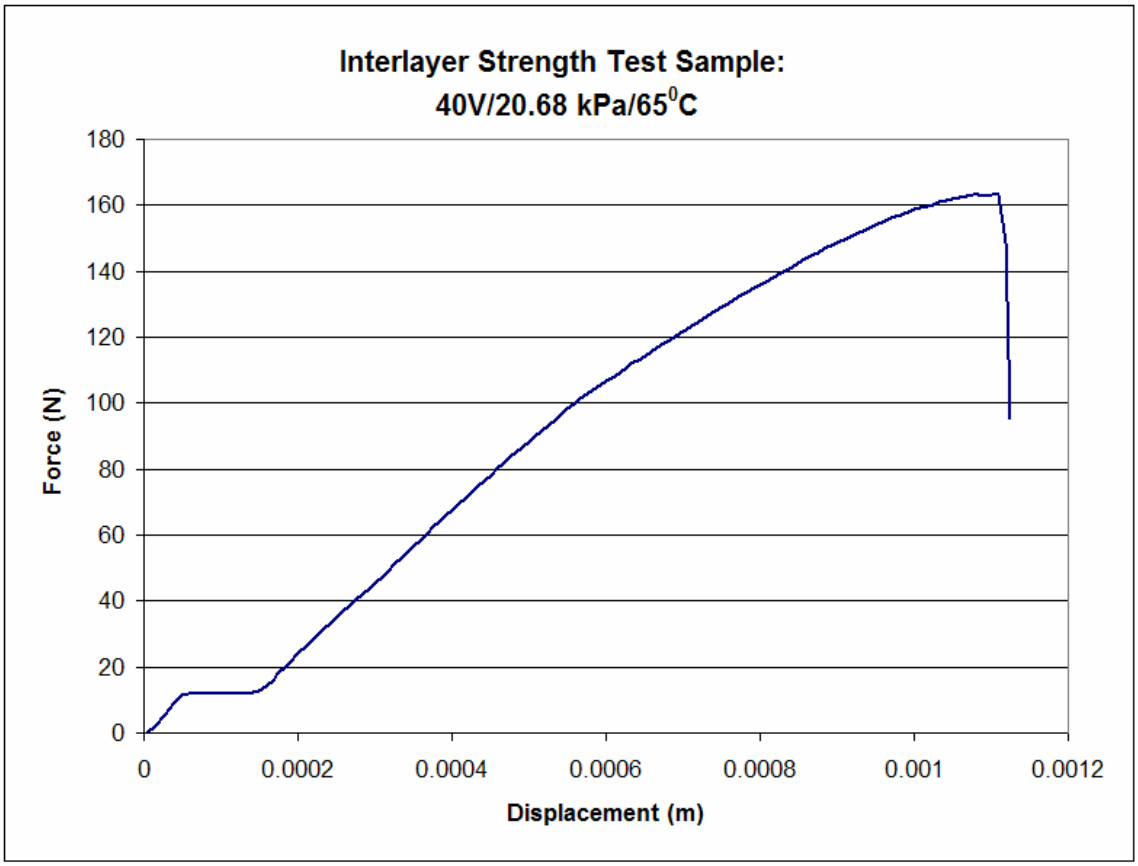

Figure 26. Sample of force-displacement curves from the interlayer tensile tests.

The results for the maximum stress in the transverse direction are shown in Figure 27. The published tensile strength for this material is 37.23 MPa (see Appendix A).

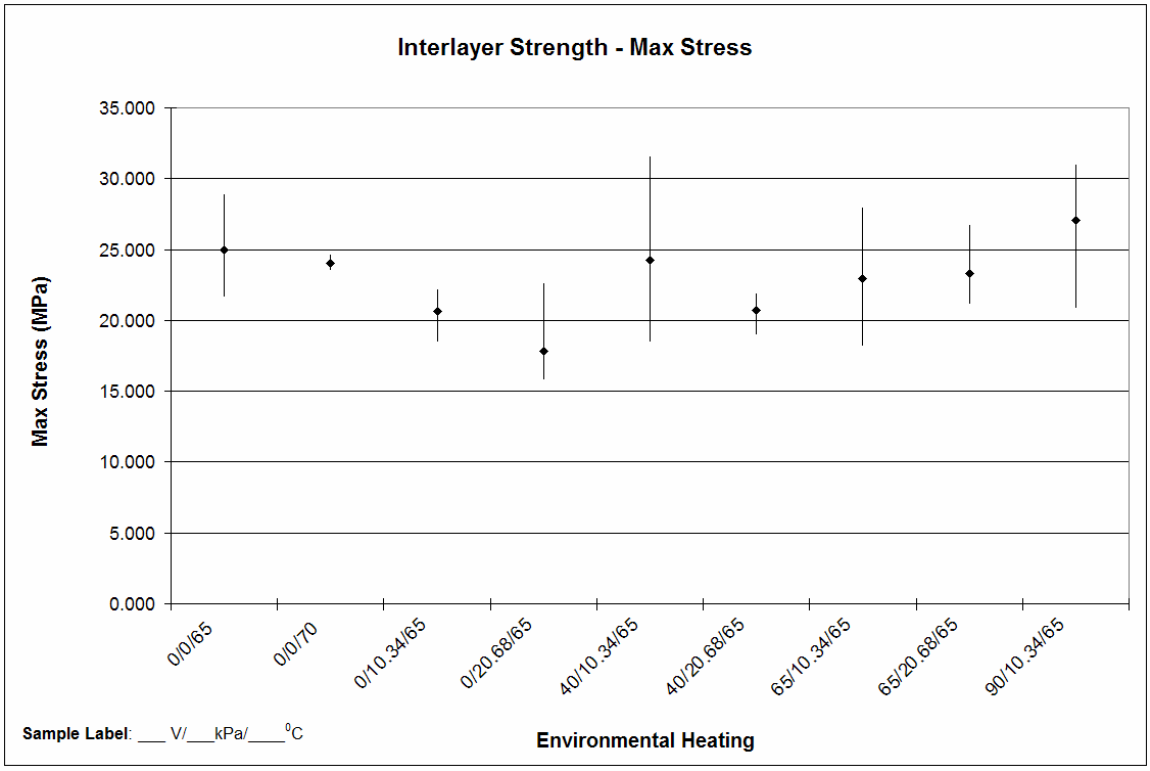

Figure 27. Maximum stress values for interlayer strength in FDM parts. Bars indicate the sample range, and the markers indicate the average value over the sample group.

Table 10. ANOVA table for one-factor analysis of interlayer strength.

ANOVA (Level of significance: α=5%)

Source of Variation	*deg. of freedom*	*SS*	*MS*	*F*	*P-value*	*F crit*	
Env. Heating	8	300.7762	37.597	4.4907	0.000757	2.2085	*
Error	36	301.3984	8.37218				
Total	44	602.1746					

* - Significant

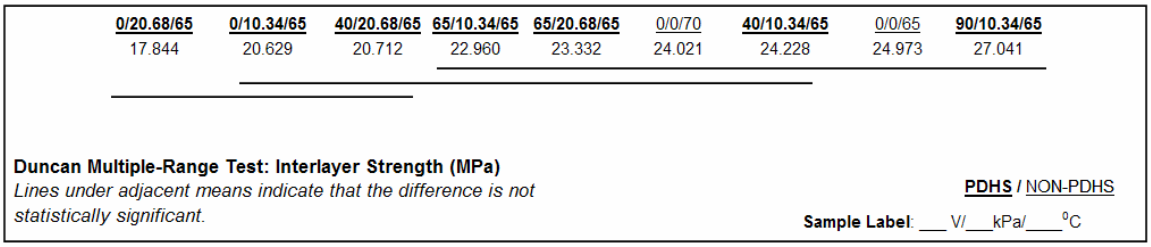

Figure 28. Duncan multiple-range test for one-factor analysis of interlayer strength.

The ANOVA table for the one-factor analysis and Duncan multiple-range test diagram are shown in Table 10 and Figure 28. The one-factor analysis of interlayer strength shows several things. First, there is a statistically significant reduction in interlayer strength for the parts made at 0V—that is, no heating of the PDHS air flow. Even more important, parts made with the PDHS do not show a statistically significant improvement in interlayer strength over parts made without the PDHS, although the group of parts made at the highest level of voltage had the highest average interlayer strength.

The ANOVA table for the two-factor analysis for interlayer strength is shown in Table 11. The table shows that, as with the other analyses, the only significant treatment is PDHS voltage. The Duncan multiple-range test for the different voltage groups is shown in Figure 29.

Table 11. ANOVA table for two-factor analysis of interlayer strength.

ANOVA (Level of significance: α=5%)

Source of Variation	*Deg. of freedom*	*Sum of Squares*	*Mean Square*	*F*	$F_{critical}$	
Replication	*4*	*20.4671*	*5.11678*	*0.5751*	*2.87*	
Main Effects:						
Voltage	*2*	*93.6996*	*46.8498*	*5.2657*	*3.49*	* - Significant
Air press.	*1*	*33.3855*	*33.3855*	*3.7524*	*4.35*	
Interaction	*2*	*16.9251*	*8.46255*	*0.9512*	*3.49*	
Error	*20*	*177.9421*	*8.8971*			
Total	*29*	*342.4194*				

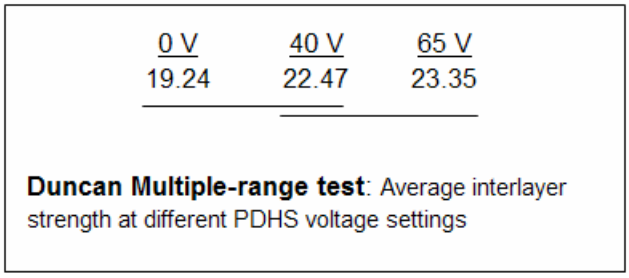

Figure 29. Duncan multiple-range test using different PDHS voltages (average strength shown in MPa).

The results from the ANOVA analysis are summarized in Table 12 and Table 13.

Table 12. Summary of one-factor analyses.

Variable	One-factor Analysis: *Environmental Heating*	Notes
Dimensional Accuracy	Significant	Parts made at 90V had significantly higher deviation than non-PDHS parts.
Flexural Strength	Significant	Parts made at 90V had significantly lower strength than all others.
Interlayer Strength	Significant	Parts made at 0V with PDHS air flow had significantly lower strength. PDHS parts did not have higher strength than non-PDHS parts.

Table 13. Summary of two-factor analyses.

Variable	Two-Factor Analysis		Notes
	Voltage	*Air Pressure*	
Dimensional Accuracy	Significant	Not Significant	Parts made at 65V had higher deviation than parts made at 0V.
Flexural Strength	Not Significant	Not Significant	
Interlayer Strength	Significant	Not Significant	Parts made at 65V had higher strength than parts made at 0V.

SEM Photography

In order to gain additional understanding of the effects of the PDHS, images of the fracture surfaces of a group interlayer tensile test specimens were taken using scanning electron microscopy (SEM). The three samples were parts from the strongest and weakest of the PDHS treatment groups (0V/20.68 kPa/65^0 C, 90V/10.34 kPa/65^0 C) and a non-PDHS part (0V/0 kPa/70^0 C). The set of figures below shows the fracture surface of each of the parts at x65 magnification. To assist in visualizing the surface of the specimen, it is helpful to remember that the deposited roads (which are oriented in the vertical direction in the images) have an elliptical cross-section. Thus, the fracture surface of the part will show creases where roads in one layer bond with each other. The bond surfaces show as distinct sections in-between creases where roads in adjacent layers bonded to each other. At x65 magnification, it is apparent that the approximate width of bond section is the same for all three specimens—that is, the

differences in interlayer strength does not seem to be caused by differing magnitudes of bonding surface area.

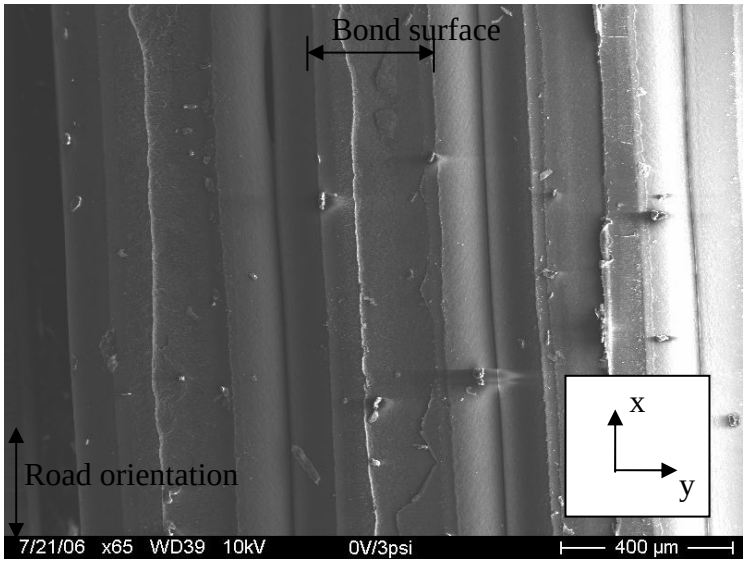

Figure 30. SEM image, at x65 magnification, of the fracture surface of part fabricated at 0V/20.68 kPa/65^0 C.

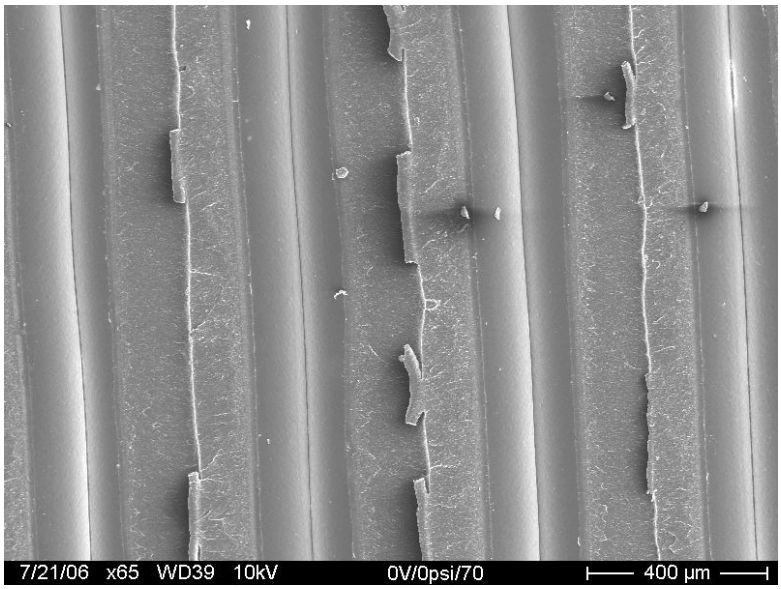

Figure 31. SEM image, at x65 magnification, of the fracture surface of a part fabricated at 0V/0 kPa/70^0 C.

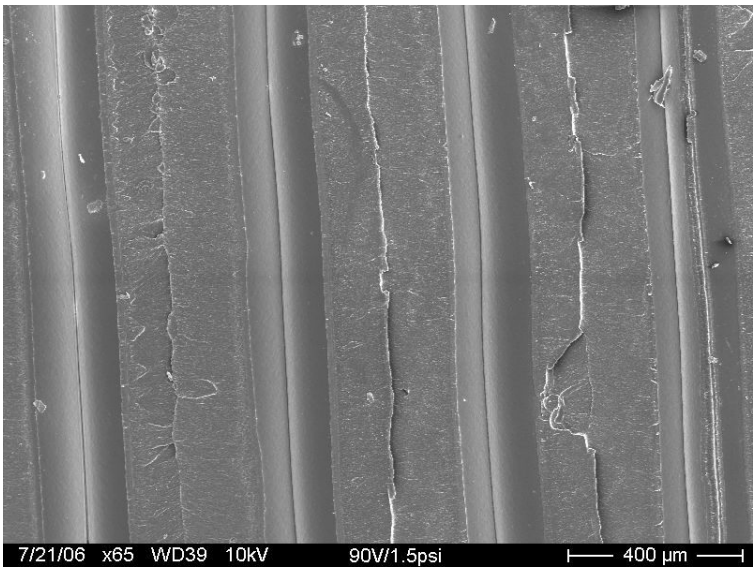

Figure 32. SEM image, at x65 magnification, of the fracture surface of a part fabricated at 90V/10.34 kPa/65^0 C.

The next set of images shows magnifications of the bonding surface of all three parts.

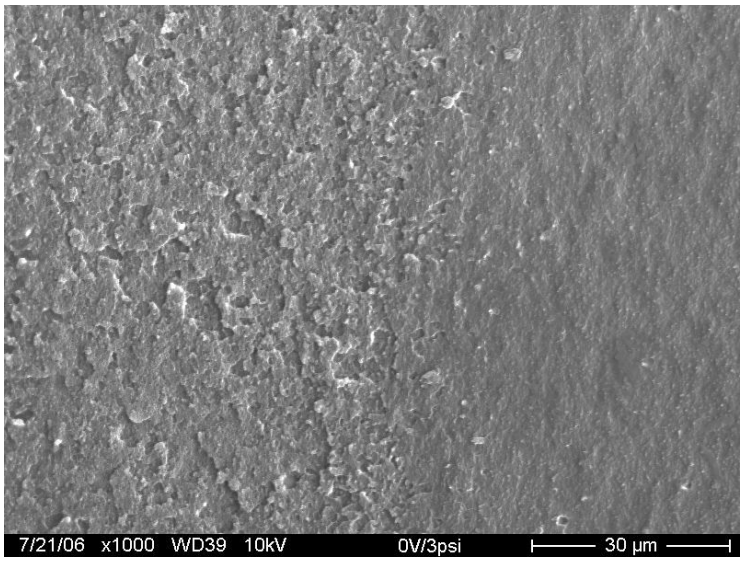

Figure 33. SEM image, at x1000 magnification, of the bonding surface of a part fabricated at 0V/20.68 kPa/65^{0}C.

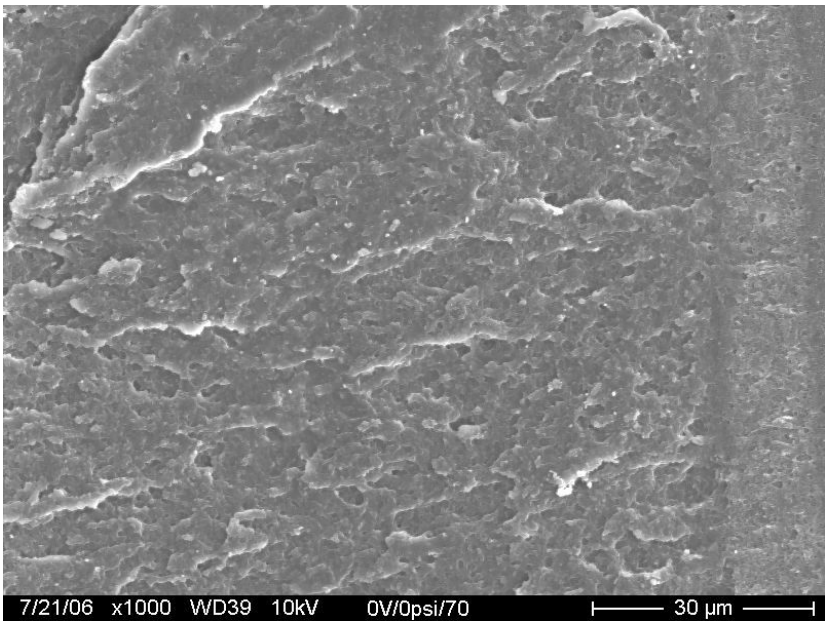

Figure 34. SEM image, at x1000 magnification, of the bonding surface of a part fabricated at 0V/0 kPa/70^{0}C.

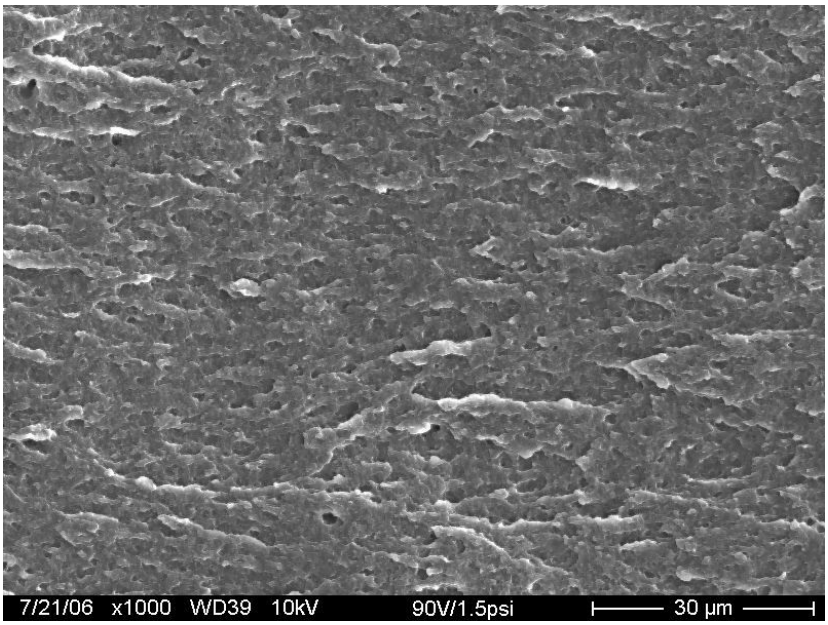

Figure 35. SEM image, at x1000 magnification, of the bonding surface of a part fabricated at 90V/10.34 kPa/65^{0}C.

The goal of the PDHS was to increase the amount of bonding taking place at the bonding interface. It was hypothesized that the greater the degree of bonding at the interface, the more material yielding there would be at the bond surface, which would result in a rougher appearance of the bonding surface. Therefore, the purpose of taking these images was to see if the bonding surfaces of the three samples had significant differences in appearance that would indicate greater (or lesser) degrees of bonding. However, an examination of these images does not reveal major differences between samples. The detailed image of the bonding surface of the in the 0V/20.68 kPa/65^{0}C part (Figure 33) contains a region that is slightly smoother than the other parts (Figure 34, Figure 35), which may account for its lower strength. However, more analysis is needed before definitive conclusions can be made. In summary, the SEM images support the conclusions of the ANOVA analysis—namely, that the PDHS does not seem to increase the amount of bonding—as evidenced by a lack of difference in appearance between parts. Additional SEM images, especially from different orientations, would provide a more thorough basis for analysis.

Additional Testing

After the experiment was conducted, some additional parts were run without the PDHS with an envelope temperature of 40^0 C (104^0 F). The intent of this set of parts was to "bracket" the experiment by further investigating the effects of envelope temperature on FDM part properties. The results are shown in the next figures, along with the earlier data from the experiment. In additional to the minimum, maximum, and average value

for each of the tests, a Duncan multiple-range test diagram is given to illustrate how this set of parts fits into the rest of the data. However, it must be noted that these parts were not produced as part of the experiment, and so additional bias may be present in the results.

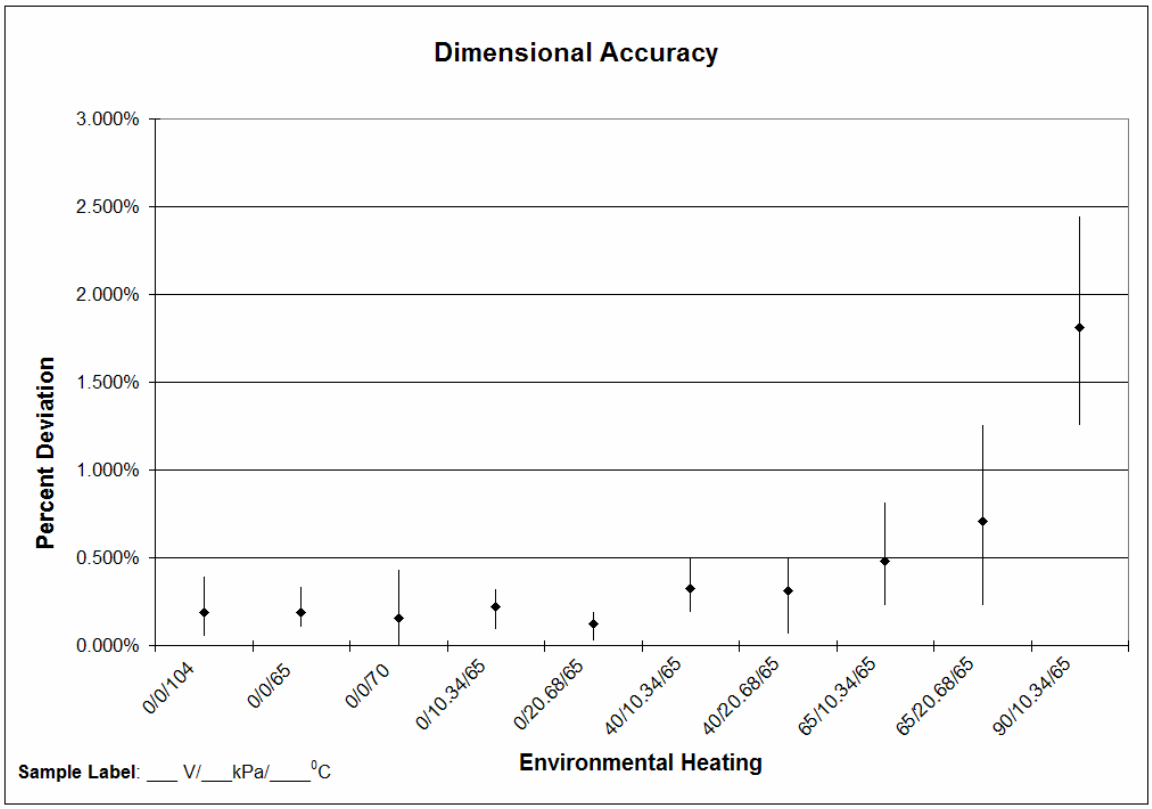

0/20.68/65	0/0/70	0/0/104	0/0/65	0/10.34/65	40/20.68/65	40/10.34/65	65/10.34/65	65/20.68/65	90/10.34/65
0.123%	0.157%	0.187%	0.189%	0.221%	0.315%	0.323%	0.480%	0.709%	1.813%

Duncan Multiple-Range Test: Dimensional Accuracy, Percent deviation
Lines under adjacent means indicate that the difference is not statistically significant.

PDHS / NON-PDHS

Sample Label: ___ V/___kPa/____°C

Figure 36. Dimensional accuracy for all samples.

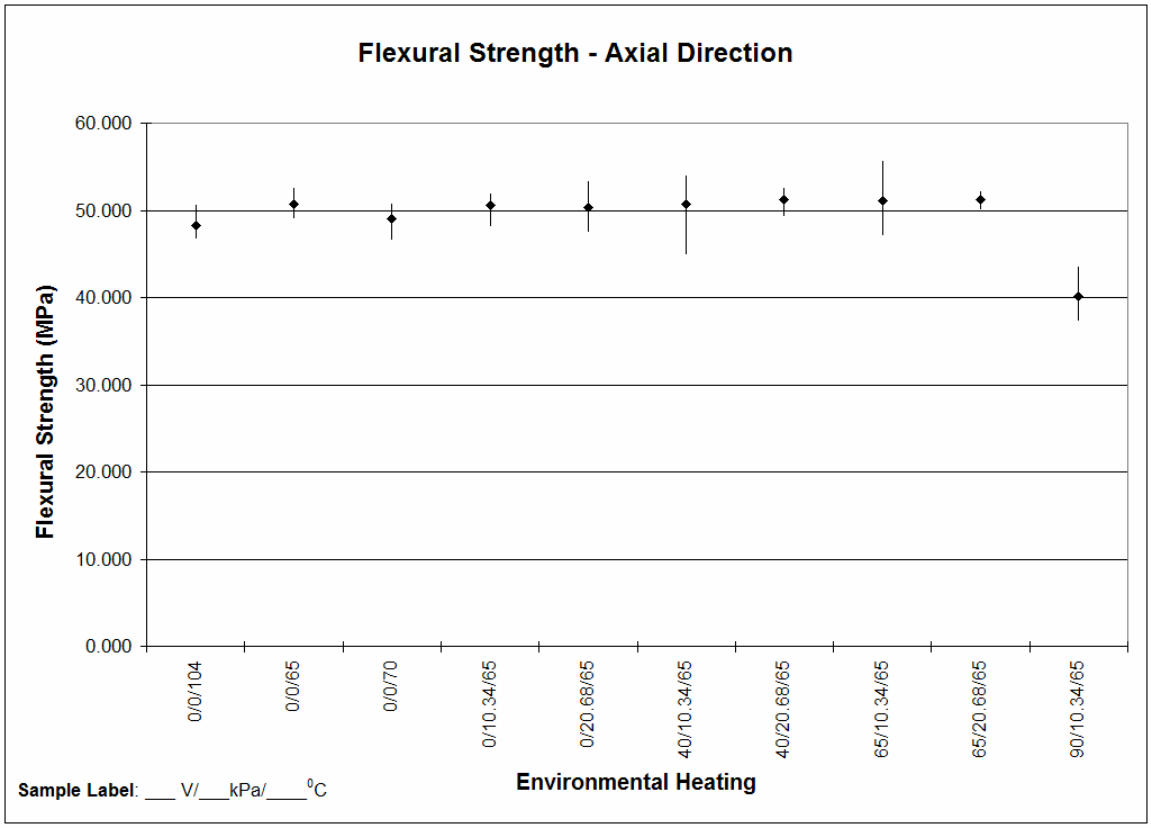

90/10.34/65	0/0/104	0/0/70	0/20.68/65	0/10.34/65	0/0/65	40/10.34/65	65/10.34/65	40/20.68/65	65/20.68/65
40.115	48.319	49.031	50.323	50.571	50.687	50.770	51.146	51.173	51.211

Duncan Multiple-Range Test: Flexure strength (MPa)

Lines under adjacent means indicate that the difference is not statistically significant.

PDHS / NON-PDHS

Sample Label: ___ V/___kPa/____°C

Figure 37. Flexure strength in the axial direction for all samples.

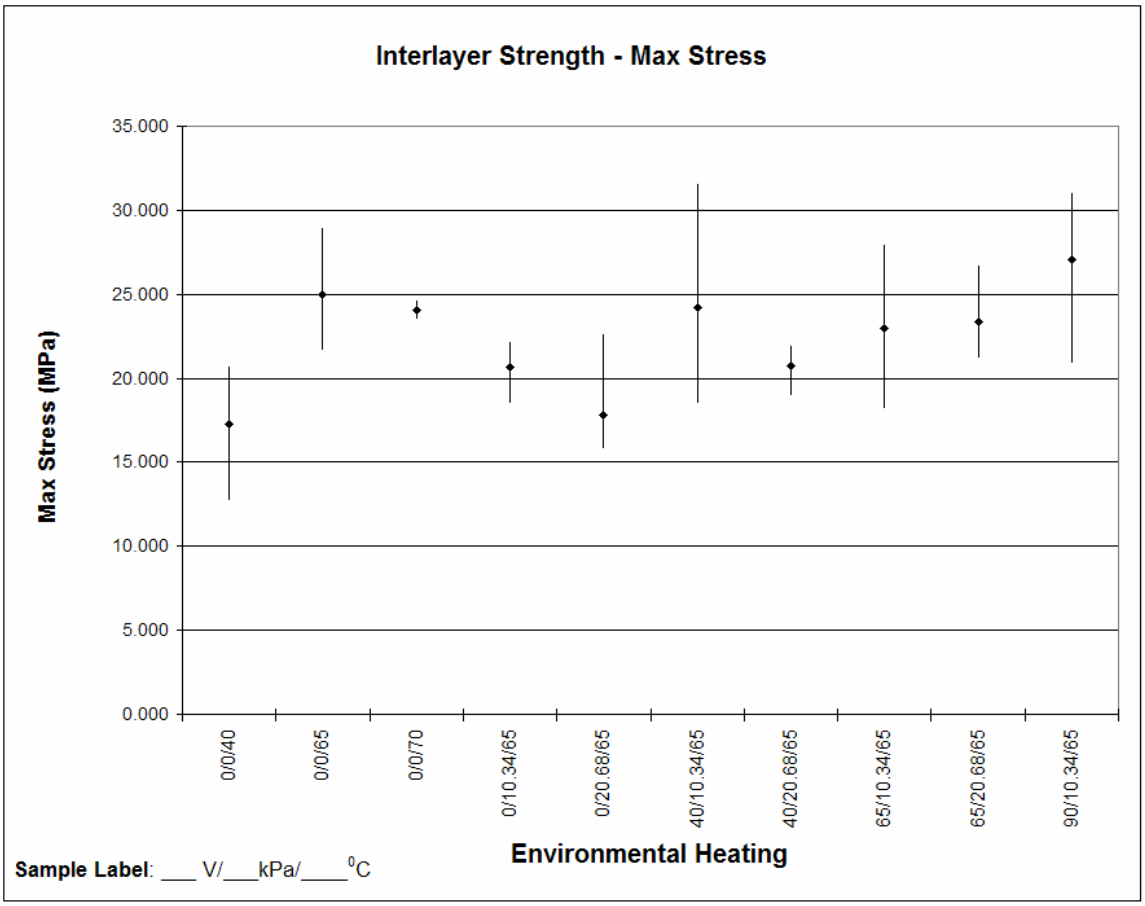

0/0/40	0/20.68/65	0/10.34/65	40/20.68/65	65/10.34/65	65/20.68/65	0/0/70	40/10.34/65	0/0/65	90/10.34/65
17.237	17.844	20.629	20.712	22.960	23.332	24.021	24.228	24.973	27.041

Duncan Multiple-Range Test: Interlayer Strength (MPa)
Lines under adjacent means indicate that the difference is not statistically significant.

PDHS / NON-PDHS

Sample Label: ___ V/___kPa/____°C

Figure 38. Interlayer strength of all samples.

The results from this additional testing indicate that fabricating samples at a low envelope temperature results in average dimensional accuracy and axial strength, but significantly weaker interlayer strength than the other non-PDHS samples or most of the

PDHS samples. These results are in agreement with the studies done by Yan *et al* and Rodriguez *et al* discussed at length in the introduction [30,34].

CONCLUSIONS, RECOMMENDATIONS, AND FUTURE WORK

The goal of this work was to investigate the potential for increasing FDM part strength in the transverse direction through the development and implementation of a pre-deposition heating system (PDHS). This system was built around a PVC welder designed to weld thermoplastic materials using forced air, and used a two-nozzle design to apply the heated air to the substrate material along the x-axis of the fabrication envelope. A statistical experiment was designed to test the effects of this system in three variables: interlayer part strength, dimensional accuracy, and axial flexural strength. A set of samples was fabricated and tested for each of these variables, and the data was analyzed using analysis of variance (ANOVA) techniques. Based on the results of the analysis and observations made during PDHS development, several conclusions can be drawn.

Conclusions

Based on the ANOVA analysis, the PDHS did not result in significantly stronger samples, and still showed presence of extreme anisotropy (as shown in the flexure tests). The samples that displayed the strongest interlayer strength were PDHS samples fabricated at the highest air temperature and lowest air flow, but these samples had the worst dimensional accuracy and significantly weaker axial flexural strength. The weakest parts were made when the envelope temperature was at its lowest setting (parts fabricated at 0V/0 kPa/40^{0}C) or when there was a large amount of *unheated* air flow in the envelope (parts fabricated at 0V/20.68 kPa/65^{0}C), which agrees with the findings of

Yan *et al*, who found that a large degree of air flow in the envelope significantly degraded interlayer strength [34].

Clearly, the results indicate that the PDHS did not have the intended improvements on FDM performance. However, based on observations made during the development of the PDHS, the central issue appears to be the use of forced air as the mechanism for heating the substrate—and the limitations of the PVC welder used to heat the air—rather than the concept itself. The specifications of the PDHS were that a "no-contact" heating source was necessary to keep from disrupting material deposition. At that point in the development, it was thought that the force of the air flow would not be sufficient to cause any disturbance in material deposition. However, when the air flow was applied to the substrate just in front of the nozzle, it disrupted the deposition of material, preventing the fabrication of good parts. The logical solution to this problem would be to decrease the air flow and increase the temperature in order to maintain the same amount of heat transfer to the substrate. This was attempted as far as the PVC welder would allow, but even at the lowest air flow (the setting used in the experiment) fabrication of good parts was impossible. Therefore, in order to make parts that were geometrically accurate, the air flow had to be moved away from the optimal point of application.

Another issue with the current design of the PDHS is the lack of precision in the heating. The goal of the PDHS design was to keep the heating as localized as possible to maintain the dimensional integrity of the part. However, the samples fabricated at the highest temperature showed a reduction in both dimensional accuracy and material

properties. The SEM images showed that the mesostructure of these parts was virtually identical to the non-PDHS parts, which seems to indicate that the dimensional inaccuracies resulted from aberrations on a larger scale. The area over which the heated air was applied was wide enough that each road was re-heated several times during deposition. When the air temperature was hot enough (as during fabrication of parts made at 90V), the roads were heated to the point of being softened—and thus more susceptible to disturbance from the air flows on either side of the deposition head. If the heating were more confined to the area of the substrate immediately preceding deposition, this disturbance and excess re-heating of the roads would be limited, and the dimensional integrity of the part could be maintained.

It is the opinion of the author that the concept underlying the design of the PDHS is sound, and that some form of PDHS will be necessary to improve transverse strength to the point where rapid manufacturing with FDM is feasible. The reason for this is that it is impossible to raise the envelope temperature to the point where interlayer and inter-road bonding is maximized without compromising the geometric integrity of the part. Therefore, in order for this maximum bond strength to occur, some form of localized heating must be present. Both of the shortcomings of the current system discussed in the previous two paragraphs were identified prior to selection of the hardware, but it was unknown at the time how significant these factors would be. This study is useful in demonstrating how sensitive the FDM technology is to air flows around the point of deposition, and establishes further design considerations for additional iterations of a pre-deposition heating system. These considerations will be discussed in the next section.

In addition to the lessons learned regarding the PDHS, the assessment hierarchy developed to test the effects of the PDHS is a useful product of this work. This analysis methodology is not specific to this design, and so would fit any process change aimed at increasing part strength in the transverse directions. The strengths of this analysis are that it examines several part performance variables (interlayer strength, flexural strength, and dimensional accuracy), so that transverse strength is not improved to the detriment of dimensional accuracy and material strength. In addition, the use of ANOVA analysis allows for changes in any of these variables to be examined for actual statistical significance, which lessens the risk of making conclusions that are not supported by the data. The hierarchy is summarized in more general terms in Figure 39.

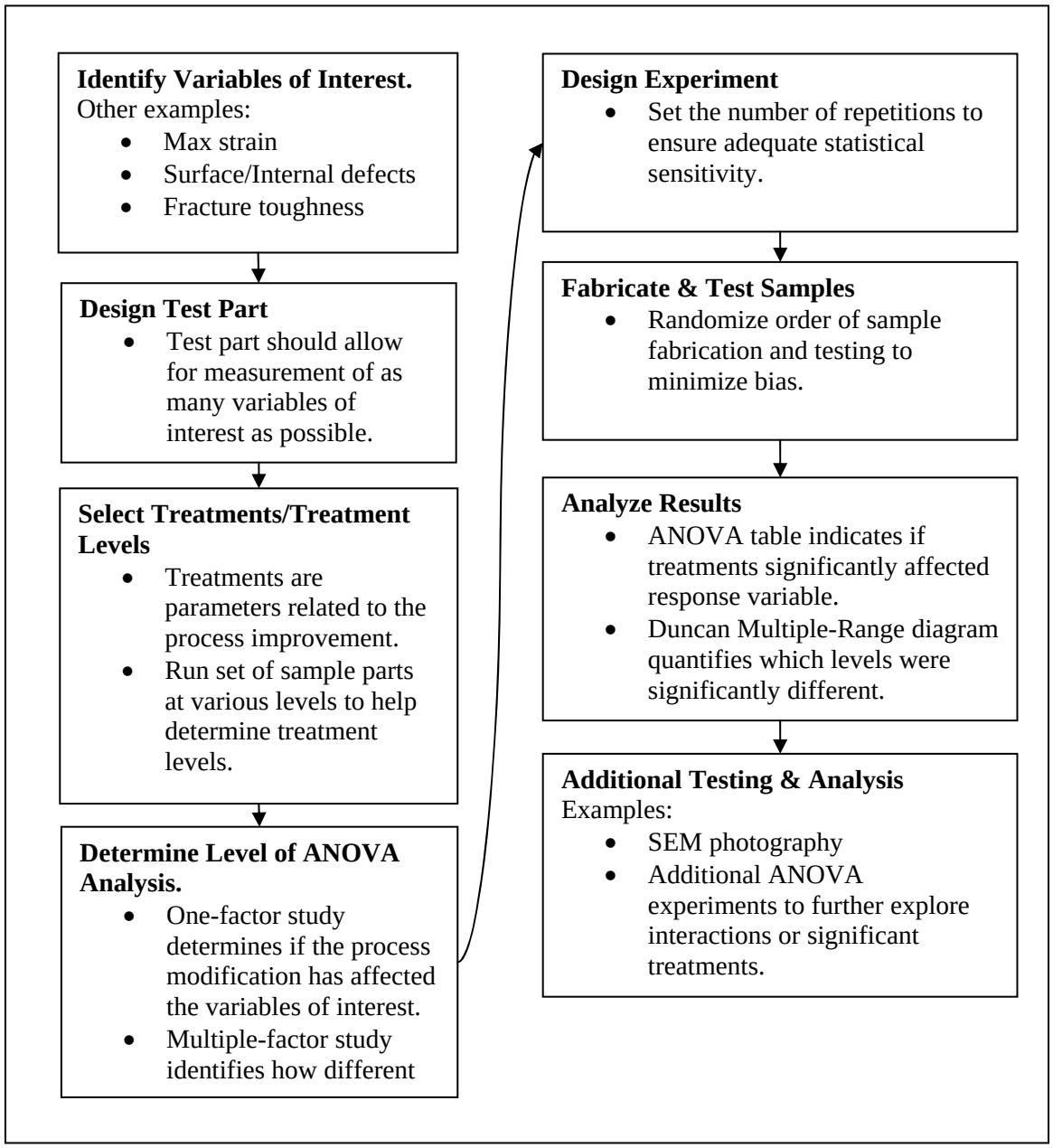

Figure 39. Testing and analysis hierarchy.

Recommendations and Future Work

Future work in this area will involve improving the design of the PDHS. Based on the results discussed in the previous section, several recommendations can be made with regard to future iterations of a pre-deposition heating system.

- Given the sensitivity of FDM to air flow, other heating technologies may be more appropriate than forced air. These may include other "no-contact" solutions, such as the other options listed in this work (or others that the author did not consider). Also, there may be some minimal-contact solutions (e.g. where contact is made with the substrate without significantly disturbing the material) that may be effective in this application.
- Additional work could be done to model and characterize the actual temperature of the substrate material at different points during deposition (prior to heating by the PDHS, after heating by the PDHS but prior to deposition, and after deposition), if further iterations of PDHS are warranted. This could include lumped parameter models or finite element models and would help set the requirements of the PDHS heating system (e.g. heat flux required to achieve the critical substrate temperature).
- In addition to modeling the process, future work should also include a study to help determine what the critical temperature of the substrate should be for to ensure bonding via molecular diffusion. As discussed in the literature review, there was some disagreement in the literature as to which material property

corresponded to the critical bonding temperature (Vicat softening temperature vs. glass transition temperature), and additional analysis should be done to resolve this question. A possible method of establishing this would be to heat treat of a set of FDM parts at different temperatures and use SEM microscopy to observe changes in the macrostructure that might indicate greater levels of molecular diffusion.

- Another recommendation would be to relax the constraint which prohibited permanent modification to the FDM machine. Having the option to make modifications to allow for easier integration between the PDHS and FDM deposition head could greatly simplify the hardware design and implementation of the PDHS.
- As discussed in the previous section, the assessment hierarchy developed in the work could be applied to any process improvement (e.g. PDHS design using microwave, process parameter changes, etc.) aimed at increasing transverse part strength without adversely affecting dimensional accuracy or material strength.

Design is an iterative process, and it is the author's hope that this work will be useful in the design of the next PDHS so that the potential of FDM in rapid manufacturing will be fulfilled.

REFERENCES CITED

1. Wohlers, T.T., Wohler's Report 2003: Rapid Prototyping, Tooling & Manufacturing State of the Industry, Annual Worldwide Progress Report, Wohlers Associates, Inc., Fort Collins, CO., p. 13. (2003)

2. Mcmains, S., "Layered Manufacturing Technologies", Communications of the ACM, Vol. 48 No. 6, p.52. (2005)

3. Bellini, A., and Guçeri, S., "Mechanical characterization of parts fabricated using fused deposition modeling", *Rapid Prototyping Journal*, Vol. 9 No. 4, pp. 252-264. (2003)

4. [3], p. 262.

5. [2], p. 53.

6. [1], p. 113.

7. Stratasys, Inc (ed.). "Fast Build options". *QuickSlice v. 5.0 Help Guide*. (1997)

8. Stratasys, Inc (ed.) "Slicing an STL file", *QuickSlice v. 5.0 Help Guide.* (1997)

9. [2], p. 52.

10. [2], p. 53.

11. [1], p. 265.

12. Bellini, A., Shor, L. and Guçeri, S., "New developments in fused deposition modeling of ceramics", *Rapid Prototyping Journal*, Vol. 11 No.4, pp. 214-220. (2005)

13. Masood, S.H., and Song, W.Q., "Development of new metal/polymer materials for rapid tooling using Fused deposition modelling", *Materials and Design*, No. 25, pp.587-594. (2004)

14. Yan, Y., Rendong, W., et. al., "Biomaterial forming research using RP technology", *Rapid Prototyping Journal*, Vol. 9 No. 3, pp.142-149. (2003)

15. Grimm, T., "Fused Deposition Modelling: A Technology Evaluation", *Time Compression Technologies*, Vol. 2 No. 2, pp. 1-6. (2003)

16. [15], p.5.

17. Agarwala, M., Jamalabad, V., et. al., “Structural quality of parts processed by fused deposition”, *Rapid Prototyping Journa*l, Vol. 2 No. 4, pp. 4-19. (1996)

18. Han, W., Jafari, M.A., Danforth, S.C. and Safari, “Tool path-based deposition planning in fused deposition processes”, *Transactions of The ASME Journal of Manufacturing Science and Engineering*, Vol. 124, pp. 462-72. (2002)

19. Han, W., Jafari, M., and Seyed, K. (2003), “Process speeding up via deposition planning in fused deposition-based layered manufacturing processes”, *Rapid Prototyping Journal*, Vol. 9 No. 4, pp. 212-218.

20. Langrana, N., Qiu, D., et. al., “Virtual simulation and video microscopy for fused deposition methods”, *Material and Design*, No. 21, pp.75-82. (2000)

21. Anitha, R., Arunachalam, S., Radhakrishnan, P., (2001), “Critical parameters influencing the quality of prototypes in fused deposition modelling” Journal *of Materials Processing Technology*. Vol 118, pp. 385-388. (2001)

22. Bose, S., Darsell, J., et. al. (2002), “Pore size and pore volume effects on alumina and TCP ceramic scaffolds”, *Material Science and Engineering*, C 23, pp. 479-486. (2002)

23. Darsell, J., Susmita, B., et. al., “From CT Scan to Ceramic Bone Graft”, *Journal of American Ceramic Society*, Vol. 86 No. 7, pp. 1076-80. (2003)

24. Shofner, M.L., Lozano, K., Rodriguez-Macias, F.J., and Barrera, E.V., “Nanofiber-Reinforced Polymers Prepared by Fused Deposition Modeling”, *Journal of Applied Polymer Science,* Vol. 89, pp.3081-3090. (2002)

25. Wu, G., Langrana, N.A., Sadanji, R., and Danforth, S., “Solid freeform frabrication of metal components using fused deposition of metals”, *Materials and Design*, Vol. 23, pp.97-105. (2002)

26. Yan, Y., Rendong, W., et. al., “Biomaterial forming research using RP technology”, *Rapid Prototyping Journal*, Vol. 9 No. 3, pp.142-149. (2003)

27. Bellini, A., and Guçeri, S., “Mechanical characterization of parts fabricated using fused deposition modeling”, *Rapid Prototyping Journal*, Vol. 9 No. 4, pp. 252-264. (2003)

28. Rodriguez, J.F., Thomas, J.P. and Renaud, J.E., "Characterizing the microstructure of fused deposition polymer components", *CAE and Intelligent Processing of Polymeric Materials*, MD-Vol. 79, ASME, NY, pp.299-308. (1997)

29. Rodriguez, J.F., Thomas, J.P., and Renaud, J.E., "Characterization of the mesostructure of fused-deposition acrylonitrile-butadience-styrene materials", *Rapid Prototyping Journal*, Vol. 6 No. 3, pp.175-185. (2000)

30. Rodriguez, J.F., Thomas, J.P. and Renaud, J.E., "Tailoring the mechanical properties of fused-deposition manufactured components", *Proc. Rapid Prototyping and Manufacturing '99*, Vol. 3, Society of Manufacturing Engineers, Dearborn, MI, pp.629-43. (1999)

31. Rodriguez, J.F., Thomas, J.P. and Renaud, J.E., "Mechanical behavior of acrylonitrile butadience styrene fused deposition materials modeling", *Rapid Prototyping Journal*, Vol. 9 No. 4, pp.219-230. (2003)

32. Rodriguez, J.F., Thomas, J.P. and Renaud, J.E., "Design of Fused-Deposition ABS Components for Stiffness and Strength", *Journal of Mechanical Design*, Vol. 125, pp.545-551. (2003)

33. Kulkarni, P., and Dutta, D. (1999), "Deposition Strategies and Resulting Part Stiffnesses in Fused Deposition Modeling", ASME Journal of Manufacturing Science and Engineering, Vol. 121, pp. 93-101.

34. Yan, Y., Zhang, R., Guodong, H., and Yuan, X., "Research on the bonding of material paths in melted extrusion modeling", *Materials and Design*, Vol. 21, pp. 93-99. (2000)

35. Rodriguez, J.F., Thomas, J.P. and Renaud, J.E., "Tailoring the mechanical properties of fused-deposition manufactured components", *Proc. Rapid Prototyping and Manufacturing '99*, Vol. 3, Society of Manufacturing Engineers, Dearborn, MI, p. 630 (1999)

36. Yan, Y., Zhang, R., Guodong, H., and Yuan, X., "Research on the bonding of material paths in melted extrusion modeling", *Materials and Design*, Vol. 21, pp. 93-99. (2000)

37. [21], p.631

38. [25], p.95

39. Automation Creations (ed.), *Matweb* (2006)

<http://www.matweb.com/search/SpecificMaterial.asp?bassnum=O1105>

40. Yardimci, M.A. and Güceri, S., "Conceptual framework for the thermal process modelling of fused deposition" *Rapid Prototyping Journal*, Vol. 2 No. 2, pp. 26-31. (1996)

41. Bird, R.B., Stewart, W.E., and Lightfoot, E.N., Transport Phenomena 2nd ed. New York: John Wiley & Sons, Inc. (2002)

42. [21], p.642

43. TWI Ltd (ed.), "TWI Knowledge Summary: Laser welding of plastics*", TWI World Centre for Materials Joining Technology*. (2006) Retrieved June 14, 2006, from
<http://www.twi.co.uk/j32k/protected/band_3/ksab002.html>

44. Froment, Ian. "Ultrasonic welding of thermoplastics - a guide to best practice", *TWI World Centre for Materials Joining Technology*. (2006) Retrieved June 16, 2006 from
<http://www.twi.co.uk/j32k/protected/band_8/bpuwts01.html>

45. Cundy, V. Personal communication. May 11, 2006.

46. ASTM D638-02a, "Standard Test Method for Tensile Properties of Plastics", American Society for Testing and Materials, Conshohocken, PA. (2003)

47. Freund, John E. and Miller, Irwin. Miller and Freund's Probability and Statistics for Engineers. Richard A. Johnson -6th ed. Upper Saddle River, NJ: Prentice-Hall, Inc. p. 396. (2000)

48. Schillings, P. Lecture notes. October 16, 2001.

49. [36], p. 395.

50. Munson, B.R., Young, D.F, and Okiishi, T.H. Fundamentals of Fluid Mechanics. 4th ed. John Wiley & Sons, Inc. p.832. (2002)

51. ASTM D790, "Standard Test Method for Flexure Properties of Plastsics", American Society for Testing and Materials, Conshohocken, PA. (2003)

APPENDICES

APPENDIX A

EQUIPMENT, MATERIAL INFORMATION

PVC Welding Kit used in the pre-deposition heating system (PDHS):

PVC WELDING KIT

Model 41592

ASSEMBLY AND OPERATING INSTRUCTIONS

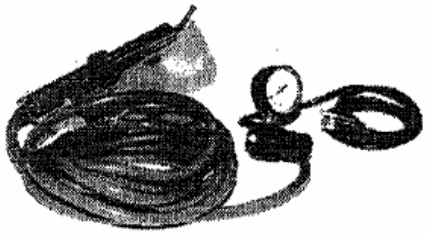

HARBOR FREIGHT TOOLS

3491 Mission Oaks Blvd., Camarillo, CA 93011

Visit our Web site at http://www.harborfreight.com

For technical questions and replacement parts, please call 1-800-444-3353

Rev 07/01

Material Properties for P500 MABS (from Stratasys Corp.):

Material Specifications*

The material specifications for P500 MABS (methyl methacrylate-acrylonitrile-butadiene-styrene) are radiation dose dependent. P500 MABS meets all FDA USP Class VI requirements and can be gamma sterilized with negligible discoloration. The property specifications below are taken from ASTM injection molded samples.

	Radiation (Mrad)		
Properties	0	2.5	5.0
Tensile strength (psi)	5,400	5,450	5,400
Tensile modulus (psi)	286,000	289,000	315,000
Flexural strength (psi)	8,500	8,500	8,600
Flexural modulus (psi)	257,000	257,000	260,000
Notched Izod 1/8 inch (ft-lb/in)	3.3	3.0	2.7
HDT 1/2 inch, (deg C. at 66 psi)	93.5	93.5	90.3
Yellow index	1.5	8.5	12.0

Recommended FDM Settings for P500 MABS (from Stratasys Corp.):

P500 - Plastic Material MABS

FDM System Parameters	FDM Tip Inner Diameter			
	0.012"	0.025"		
Speed inches/sec (recommended)	**0.800**	**0.800**		
Road Height (maximum)	0.016"	0.020"		
(minimum)	0.004"	0.006"		
(recommended)	**0.010"**	**0.010"**		
Road Width (maximum)	0.040"	0.060"		
(minimum)	0.012"	0.030"		
Liquefier Temp °C (maximum)	270	270		
(minimum)	250	250		
(recommended)	**See Spool**	**See Spool**		
Envelope Temp °C (maximum)	70	70		
(recommended)	70	70		
Room Temp °F (maximum)	82	82		

It is recommended to use the parameter values indicated in bold for perimeter roads. The values in this table may also be applied to fill and support roads if desired.

APPENDIX B

ANOVA CALCULATIONS

ANOVA Calculations: Dimensional Accuracy

ANOVA: Dimensional Accuracy, One-factor analysis

Sample Label: ___V/___kPa/____^{0}C

Percent Deviation:

	Rep										
Sample	*1*	*2*	*3*	*4*	*5*	*Count*	*Sum*	*Variance*	*Max*	*Min*	*Average*
0/0/65	0.147%	0.173%	0.107%	0.333%	0.187%	5	0.0095	7.4E-07	0.333%	0.107%	0.189%
0/0/70	0.053%	0.160%	0.147%	0.000%	0.427%	5	0.0079	2.7E-06	0.427%	0.000%	0.157%
0/10.34/65	0.267%	0.160%	0.093%	0.267%	0.320%	5	0.0111	8.5E-07	0.320%	0.093%	0.221%
0/20.68/65	0.160%	0.067%	0.027%	0.187%	0.173%	5	0.0061	5.1E-07	0.187%	0.027%	0.123%
40/10.34/65	0.187%	0.467%	0.280%	0.187%	0.493%	5	0.0161	2.2E-06	0.493%	0.187%	0.323%
40/20.68/65	0.267%	0.333%	0.067%	0.413%	0.493%	5	0.0157	2.6E-06	0.493%	0.067%	0.315%
65/10.34/65	0.387%	0.227%	0.680%	0.293%	0.813%	5	0.0240	6.5E-06	0.813%	0.227%	0.480%
65/20.68/65	0.293%	0.227%	0.587%	1.187%	1.253%	5	0.0355	2.4E-05	1.253%	0.227%	0.709%
90/10.34/65	2.440%	1.747%	1.253%	2.040%	1.587%	5	0.0907	2.0E-05	2.440%	1.253%	1.813%

ANOVA (Level of significance: α=5%)

Source of Variation	*deg. of freedom*	*SS*	*MS*	*F*	*P-value*	*F crit*	
Env. Heating	8	0.00076139	9.5174E-05	14.0616691	8.9348E-09	2.22533997	*
Error	36	0.00023012	6.7683E-06				
Total	44	0.00099151					

* - Significant

Dimensional Analysis: One-factor analysis, Duncan multiple-range test:

Sample means, sorted:

Env.	Mean
0/20.68/65	0.123%
0/0/70	0.157%
0/0/65	0.189%
0/10.34/65	0.221%
40/20.68/65	0.315%
40/10.34/65	0.323%
65/10.34/65	0.480%
65/20.68/65	0.709%
90/10.34/65	1.813%

Standard error of the mean:

MSE =	6.8E-06
n =	5
s_y=	0.00116347

Values of r_p for α = .05, 36 dof [38]

p (# of means)	r_p	R_p
2	2.854	0.332%
3	3.004	0.350%
4	3.094	0.360%
5	3.164	0.368%
6	3.216	0.374%
7	3.264	0.380%
8	3.296	0.383%
9	3.326	0.387%

Sample ranges:	9	8	7	6	5	4	3	2
	1.691%	**0.587%**	**0.357%**	0.200%	0.192%	0.099%	0.067%	0.035%
		1.656%	**0.552%**	**0.323%**	0.165%	0.157%	0.064%	0.032%
			1.624%	**0.520%**	0.291%	0.133%	0.125%	0.032%
				1.592%	**0.488%**	0.259%	0.101%	0.093%
					1.499%	**0.395%**	0.165%	0.008%
						1.491%	**0.387%**	0.157%
							1.333%	0.229%
								1.104%

Bold = Range exceeds R_p, indicates significance difference between means.

0/20.68/65	0/0/70	0/0/65	0/10.34/65	40/20.68/65	40/10.34/65	65/10.34/65	65/20.68/65	90/10.34/65
0.123%	0.157%	0.189%	0.221%	0.315%	0.323%	0.480%	0.709%	1.813%

Duncan Multiple-Range Test: Dimensional Accuracy, Percent Deviation

Lines under adjacent means indicate that the difference is not statistically significant.

PDHS / NON-PDHS

Sample Label: __ V/__kPa/___°C

ANOVA Calculations: Dimensional accuracy, continued.

ANOVA: Dimensional Accuracy ~ 3 x 2 factorial study (Voltage x air pressure in PDHS)

Sample Label: ___V/___kPa/____^{0}C

Percent Deviation:

	Rep					
Sample	*1*	*2*	*3*	*4*	*5*	*Totals:*
0/10.34/65	0.267	0.160	0.093	0.267	0.320	1.1067
0/20.68/65	0.160	0.067	0.027	0.187	0.173	0.6133
40/10.34/65	0.187	0.467	0.280	0.187	0.493	1.6133
40/20.68/65	0.267	0.333	0.067	0.413	0.493	1.5733
65/10.34/65	0.387	0.227	0.680	0.293	0.813	2.4000
65/20.68/65	0.293	0.227	0.587	1.187	1.253	3.5467
Totals:	1.5600	1.4800	1.7333	2.5333	3.5467	**10.8533**

Squares

0.071	0.026	0.009	0.071	0.102	1.22
0.026	0.004	0.001	0.035	0.030	0.38
0.035	0.218	0.078	0.035	0.243	2.60
0.071	0.111	0.004	0.171	0.243	2.48
0.150	0.051	0.462	0.086	0.662	5.76
0.086	0.051	0.344	1.408	1.571	12.58
2.43	2.19	3.00	6.42	12.58	

C =	3.926494815
SST =	2.5296830
SS(Tr) =	1.0770963
SSR =	0.5110163
SSE =	0.9415704
SSA =	0.9211141
SSB =	0.0125393
SS(AB) =	0.1434430

	Air pressure (kPa)		
Voltage (V)	*10.34*	*20.68*	
0	1.1067	0.6133	1.7200
40	1.6133	1.5733	3.1867
65	2.4000	3.5467	5.9467
	5.1200	5.7333	10.8533

ANOVA (Level of significance: α=5%)

Source of Variation	*Degrees of freedom*	*Sum of Squares*	*Mean Square*	*F*	$F_{critical}$	
Replication	*4*	*0.511016*	*0.1277541*	*1.2223245*	*2.87*	
Main Effects:						
Voltage	*2*	*0.921114*	*0.460557*	*9.7827428*	*3.49*	* - Significant
Air press.	*1*	*0.012539*	*0.0125393*	*0.2663478*	*4.35*	
Interaction	*2*	*0.143443*	*0.0717215*	*1.5234439*	*3.49*	
Error	*20*	*0.941570*	*0.0470785*			
Total	*29*	*2.529683*				

Duncan multiple-range test: Dimensional accuracy, 3 x 2 factorial analysis

Voltage means:

0 V	0.172
40 V	0.319
65 V	0.595

Standard error of the mean:

MSE =	4.7E-02
n =	5
s_y=	0.097034549

From statistical table, for 20 dof [38]:

p (# of means)	r_p	R_p
2	2.95	0.28625
3	3.1	0.30081

Sample mean ranges
Bold = significant

3	2
0.4227	0.1467
	0.27600

0 V	40 V	65 V
0.172%	0.319%	0.595%

Duncan Multiple-range test: Average dimensional deviation for different PDHS Voltage settings.

ANOVA Calculations: Interlayer strength

ANOVA: Interlayer strength ~ One factor study (Environmental heating)

Sample Label: ___V/___kPa/____^{0}C

Maximum Stress (MPa):

	Rep										
Sample	*1*	*2*	*3*	*4*	*5*	*Count*	*Sum*	*Variance*	*Average*	*Max*	*Min*
0/0/65	25.3727	28.8890	24.7522	21.6495	24.2006	5	124.8641	6.8E+00	24.973	28.889	21.650
0/0/70	23.5111	24.2006	23.9938	24.6143	23.7869	5	120.1067	1.7E-01	24.021	24.614	23.511
0/10.34/65	22.1322	20.8911	18.4779	21.3048	20.3395	5	103.1456	1.9E+00	20.629	22.132	18.478
0/20.68/65	16.7543	22.6148	16.5474	15.7890	17.5127	5	89.2182	7.5E+00	17.844	22.615	15.789
40/10.34/65	24.6143	22.6148	23.9248	31.5090	18.4779	5	121.1409	2.2E+01	24.228	31.509	18.478
40/20.68/65	19.9948	21.0980	18.9606	21.6495	21.8564	5	103.5593	1.5E+00	20.712	21.856	18.961
65/10.34/65	23.9248	25.2348	27.9238	18.2022	19.5122	5	114.7977	1.6E+01	22.960	27.924	18.202
65/20.68/65	23.3732	21.1669	26.6827	22.7527	22.6838	5	116.6593	4.2E+00	23.332	26.683	21.167
90/10.34/65	30.9575	20.8911	26.1311	28.1996	29.0269	5	135.2062	1.5E+01	27.041	30.957	20.891

ANOVA (Level of significance: α=5%)

Source of Variation	*deg. of freedom*	*SS*	*MS*	*F*	*P-value*	*F crit*	
Env. Heating	8	300.7762	37.597	4.4907	0.0008	2.20852	*
Error	36	301.3984	8.37218				
Total	44	602.1746					

* - Significant

Interlayer Strength: One-factor analysis, Duncan multiple range test

Sample means, sorted:

Env.	Mean
0/20.68/65	17.844
0/10.34/65	20.629
40/20.68/65	20.712
65/10.34/65	22.960
65/20.68/65	23.332
0/0/70	24.021
40/10.34/65	24.228
0/0/65	24.973
90/10.34/65	27.041

Standard error of the mean:

MSE =	8.4E+00
n =	5
s_y=	1.294

From statistical table, for 36 dof [38]:

p	r_p	R_p
2	2.854	3.693
3	3.004	3.887
4	3.094	4.004
5	3.164	4.094
6	3.216	4.162
7	3.264	4.224
8	3.296	4.265
9	3.326	4.304

Sample ranges	9	8	7	6	5	4	3	2
	9.198	**7.129**	**6.385**	**6.178**	**5.488**	**5.116**	2.868	2.785
		6.412	**4.344**	3.599	3.392	2.703	2.330	0.083
			6.329	**4.261**	3.516	3.309	2.620	2.248
				4.082	2.013	1.269	1.062	0.372
					3.709	1.641	0.896	0.689
						3.020	0.951	0.207
							2.813	0.745
								2.068

Bold = Range exceeds R_p, significantly different.

0/20.68/65	**0/10.34/65**	**40/20.68/65**	**65/10.34/65**	**65/20.68/65**	0/0/70	**40/10.34/65**	0/0/65	**90/10.34/65**
17.844	20.629	20.712	22.960	23.332	24.021	24.228	24.973	27.041

Duncan Multiple-Range Test: Interlayer Strength (MPa)

Lines under adjacent means indicate that the difference is not statistically significant.

PDHS / NON-PDHS

Sample Label: ___ V/___kPa/____^{0}C

ANOVA Calculations: Interlayer strength, continued.

ANOVA: Interlayer strength ~ 3 x 2 factorial study (Voltage x air pressure in PDHS)

Maximum Stress (MPa)

Data:

Sample Label: ___V/___kPa/____°C

	Rep					
Sample	1	2	3	4	5	Totals:
0/10.34/65	22.1322	20.8911	18.4779	21.3048	20.3395	103.1456
0/20.68/65	16.7543	22.6148	16.5474	15.7890	17.5127	89.2182
40/10.34/65	24.6143	22.6148	23.9248	31.5090	18.4779	121.1409
40/20.68/65	19.9948	21.0980	18.9606	21.6495	21.8564	103.5593
65/10.34/65	23.9248	25.2348	27.9238	20.2022	19.5122	116.7977
65/20.68/65	23.3732	21.1669	26.6827	22.7527	22.6838	116.6593
Totals:	130.7935	133.6204	132.5172	133.2073	120.3825	**650.6209**

Squares

489.83	436.44	341.43	453.89	413.70	10639.01
280.71	511.43	273.82	249.29	306.69	7959.88
605.86	511.43	572.40	992.82	341.43	14675.11
399.79	445.12	359.50	468.70	477.70	10724.52
572.40	636.80	779.74	408.13	380.72	13641.71
546.31	448.04	711.97	517.69	514.55	13609.39
17107.0	17854.41	17560.82	17744.18	14491.94	

C =	14105.9152
SST =	342.4194
SS(Tr) =	144.0101
SSR =	20.4671
SSE =	177.9421
SSA =	93.6996
SSB =	33.3855
SS(AB) =	16.9251

	Air pressure				
Voltage	1.5	3			
0	103.1456	89.2182	192.3637	3.7E+04	
40	121.1409	103.5593	224.7001	5.0E+04	
65	116.7977	116.6593	233.4570	5.5E+04	
	341.0842	309.4367	650.5209		
	1.2E+05	9.6E+04			

ANOVA (Level of significance: α=5%)

Source of Variation	*Deg. of freedom*	*Sum of Squares*	*Mean Square*	*F*	$F_{critical}$	
Replication	4	20.4671	5.11678	0.5751	2.87	
Main Effects:						
Voltage	2	93.6996	46.8498	5.2657	3.49	* - Significant
Air press.	1	33.3855	33.3855	3.7524	4.35	
Interaction	2	16.9251	8.46255	0.9512	3.49	
Error	20	177.9421	8.8971			
Total	29	342.4194				

Duncan multiple-range test: Interlayer strength, 3 x 2 factorial analysis

Voltage means:

0 V	19.2364
40 V	22.4700
65 V	23.3457

Standard error of the mean:

MSE =	8.9E+00
n =	5
s_y=	1.333949

From statistical table, for 20 dof [38]:

p	r_p	R_p
2	2.95	3.817
3	3.1	4.011

Sample mean ranges

3	2
4.1093	3.2336
	0.8757

0 V	40 V	65 V
19.24	22.47	23.35

Duncan Multiple-range test: Average interlayer strength at different PDHS voltage settings

ANOVA Calculations: Flexural strength, axial direction

ANOVA: Flexural Strength, Axial Direction; One-factor Analysis

Sample Label: ___V/___kPa/____^{0}C

Flexural Strength (MPa)

	Rep										
Sample	*1*	*2*	*3*	*4*	*5*	*Count*	*Sum*	*Variance*	*Max*	*Min*	*Average*
0/0/65	49.029	51.267	49.592	52.492	51.055	5	253.4343	1.9E+00	52.49	49.03	50.69
0/0/70	46.895	50.406	46.559	50.605	50.688	5	245.1528	4.4E+00	50.69	46.56	49.03
0/10.34/65	51.820	51.791	48.171	51.334	49.740	5	252.8562	2.5E+00	51.82	48.17	50.57
0/20.68/65	53.308	47.517	51.296	48.096	51.396	5	251.6129	6.0E+00	53.31	47.52	50.32
40/10.34/65	52.498	49.752	53.952	44.962	52.685	5	253.8484	1.3E+01	53.95	44.96	50.77
40/20.68/65	49.239	50.700	52.556	52.271	51.100	5	255.8652	1.8E+00	52.56	49.24	51.17
65/10.34/65	47.073	51.506	50.783	55.671	50.699	5	255.7310	9.4E+00	55.67	47.07	51.15
65/20.68/65	51.994	51.292	52.112	50.011	50.644	5	256.0536	8.0E-01	52.11	50.01	51.21
90/10.34/65	43.424	37.321	38.265	40.980	40.582	5	200.5732	5.8E+00	43.42	37.32	40.11

ANOVA (Level of significance: α=5%)

Source of Variation	*SS*	*df*	*MS*	*F*	*P-value*	*F crit*	
Env. Heating	507.8048	8	63.4756	12.56326	2.14E-08	2.2085181	*
Error	181.88917	36	5.052477				
Total	689.69397	44					

* - Significant

Flexural strength, axial direction: One-factor analysis, Duncan multiple range test

Sample means, sorted:

Env.	Mean
90/10.34/65	40.115
0/0/70	49.031
0/20.68/65	50.323
0/10.34/65	50.571
0/0/65	50.687
40/10.34/65	50.770
65/10.34/65	51.146
40/20.68/65	51.173
65/20.68/65	51.211

Standard error of the mean:

MSE =	5.1E+00
n =	5
s_y=	1.005234

From statistical table, for 36 dof [38]:

p	r_p	R_p
2	2.854	2.869
3	3.004	3.020
4	3.094	3.110
5	3.164	3.181
6	3.216	3.233
7	3.264	3.281
8	3.296	3.313
9	3.326	3.343

Sample ranges	9	8	7	6	5	4	3	2
	11.096	**11.058**	**11.032**	**10.655**	**10.572**	**10.457**	**10.208**	**8.916**
		2.180	2.142	2.116	1.739	1.656	1.541	1.292
			0.888	0.850	0.824	0.447	0.364	0.249
				0.639	0.602	0.575	0.198	0.116
					0.524	0.486	0.459	0.083
						0.441	0.403	0.377
							0.065	0.027
								0.038

Bold = Range exceeds R_p, significantly different.

90/10.34/65	0/0/70	**0/20.68/65**	**0/10.34/65**	0/0/65	**40/10.34/65**	**65/10.34/65**	**40/20.68/65**	**65/20.68/65**
40.115	49.031	50.323	50.571	50.687	50.770	51.146	51.173	51.211

Duncan Multiple-Range Test: Flexure Strength, Axial direction (MPa)

Lines under adjacent means indicate that the difference is not statistically significant.

PDHS / NON-PDHS

Sample Label: ___V/___kPa/___^{0}C

ANOVA Calculations: Flexural strength, axial direction, continued.

ANOVA: Flexural Strength, Axial direction; 3 x 2 factorial study (Voltage x air pressure in PDHS)

Flexural Strength (MPa)

Data:

Sample Label: ___V/___kPa/____^{0}C

	Rep					
Sample	*1*	*2*	*3*	*4*	*5*	*Totals:*
0/10.34/65	51.8202	51.7911	48.1706	51.3339	49.7404	252.8562
0/20.68/65	53.3081	47.5167	51.2958	48.0964	51.3958	251.6129
40/10.34/65	52.4983	49.7517	53.9517	44.9617	52.6850	253.8484
40/20.68/65	49.2390	50.6996	52.5559	52.2706	51.1001	255.8652
65/10.34/65	47.0729	51.5056	50.7833	55.6708	50.6985	255.7310
65/20.68/65	51.9941	51.2924	52.1121	50.0111	50.6439	256.0536
Totals:	305.9327	302.5572	308.8693	302.3444	306.2637	1.5260E+03

Squares

2685.34	2682.32	2320.40	2635.17	2474.10	63936.25
2841.76	2257.84	2631.26	2313.27	2641.53	63309.07
2756.08	2475.24	2910.78	2021.55	2775.71	64439.02
2424.48	2570.45	2762.12	2732.22	2611.22	65467.00
2215.85	2652.82	2578.94	3099.23	2570.34	65398.32
2703.39	2630.91	2715.67	2501.11	2564.81	65563.46
9.36E+04	9.15E+04	9.54E+04	9.14E+04	9.38E+04	

C =	77619.21	
SST =	136.6956	7.409147
SS(Tr) =	3.4154	2.9024
SSR =	5.0452	0.3982
SSE =	128.2351	4.1085
SSA =	2.8437	1.8368
SSB =	0.0401	0.6163
SS(AB) =	0.5317	0.4492

	Air pressure		
Voltage	*1.5*	*3*	
0	252.8562	251.6129	504.4691
40	253.8484	255.8652	509.7136
65	255.7310	256.0536	511.7846
	762.4356	763.5318	1525.9673

ANOVA (Level of significance: a=5%)

Source of Variation	*Degrees of freedom*	*Sum of Squares*	*Mean Square*	*F*	$F_{critical}$
Replication	*4*	*5.0452*	*1.2613*	*0.2754*	*2.87*
Main Effects:					
Voltage	*3*	*2.8437*	*0.9479*	*0.207*	*3.49*
Air press.	*1*	*0.0401*	*0.0401*	*0.0087*	*4.35*
Interaction	*3*	*0.5317*	*0.1772*	*0.0387*	*3.49*
Error	*28*	*128.2*	*4.5798*		
Total	*39*	*136.7*			

APPENDIX C

EXIT FLOW RATE CALCULATIONS

FLOW RATE ANALYSIS

System description: The system is divided into three sections: a section of flexible plastic tubing (A), followed by a section of copper tubing (B), after which the flow is split into two sections of brass tubing (C). The pressure is known at point 1, and the desired quantity is the flow rate at the exit point of the brass tubes.

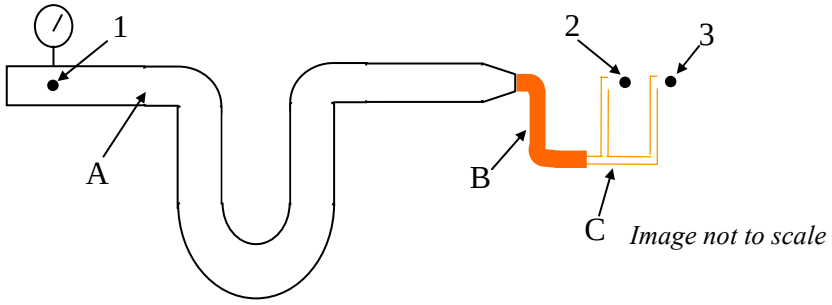

Assumptions:

1. Air will be treated as incompressible, due to the small change in pressure.
2. Negligible change in elevation.
3. The image below approximates the geometry of the system during deposition (for the purposes of calculating minor losses).
4. In determining the head loss for the brass tubing sections, the difference in length between the section leading to Point 2 (section II) is approximately the same as the section leading to point 3 (section III). Due to the relatively small lengths of this section and the small difference between lengths, the difference in head loss due to the slightly longer length of section III is expected to be negligible.
5. Points 2 & 3 are points located on a streamline from 1. Points 2,3 are far enough away from the exit points for the velocity at 2,3 to be negligible relative to the velocities in the tubing[1].
6. As a simplifying assumption, the heat transfer in this system will be neglected. For the purposes of this study, only an approximate estimate of exit flow rate is needed. The analysis will be run for one air pressure setting using the properties for air at room temperature (20^0C) as well as the highest deposition temperature (200^0C) to see how the change in air properties affects the flow rate.

[1] Janna, W. Introduction to Fluid Mechanics. 3rd ed. PWS-Kent Publishing Co. (1993) p.255

FLOW RATE ANALYSIS, cont.

Assumptions, cont.

7. Due to varying lengths and minor losses, the exit flow rate will be slightly different between the two brass tubes. For the purpose of this analysis, which is to get an approximate estimate of the flow rate, the exit flow rate will be characterized by the tube corresponding to point 2.

Material properties, System parameters:

Values for material roughnesses, minor losses, and Moody diagram (for friction factors) were taken from: Munson, Young, & Okiishi. Fundamentals of Fluid Mechanics. 4th ed. John Wiley & Sons. (2002) pp.443-512.

A: Plastic Hose, Mat'l Props[2]

$D_A = 0.0127 \cdot m$

$A_A = 1.267 \times 10^{-4} \cdot m^2$

$\varepsilon_A = 0.00 \cdot m$

$L_A = 3.048 \cdot m$

Minor Losses

2 x 90^0 Elbows (non-threaded): $K_L = 0.6$
180^0 Return bend: $K_L = 0.2$
$\Sigma K_{LA} = 0.8$

B: Copper Tubing, Mat'l Props

$D_B = .00635 \cdot m$

$A_B = 3.166 \times 10^{-5} \cdot m^2$

$\varepsilon_B = 1.524 \times 10^{-5} \cdot m$

$L_B = .127 \cdot m$

Minor Losses

Convergent outlet: $D_B/D_A = 0.5$: $K_L = 0.05$
2 x 90^0 Elbows (non-threaded): $K_L = 0.6$
$\Sigma K_{LB} = 0.65$

C: Brass Tubing, Mat'l Props

$D_C = 3.175 \times 10^{-3} \cdot m$

$A_C = 7.917 \times 10^{-6} \cdot m^2$

$\varepsilon_C = 1.524 \times 10^{-5} \cdot m$

$L_C = .03175 \cdot m$

Exit:

$D_E = 1.27 \times 10^{-3} \cdot m$

$A_E = 1.26 \times 10^{-6} \cdot m^2$

Common:

Minor Losses

Sudden contraction, $A_C/A_B = 0.25$: $K_L = 0.42$
90^0 Elbow (non-threaded): $K_L = 0.3$
Sudden contraction, $A_E/A_C = 0.25$: $K_L = 0.47$
Exit: $K_L = 1.0$

Path 1-2:

Tee, branch flow: $K_L = 1.0$
$\Sigma K_{LC(1-2)} = 3.19$

Path 1-3:

Tee, line flow: $K_L = 0.2$
90^0 Elbow (non-threaded): $K_L = 0.3$
$\Sigma K_{LC(1-2)} = 2.69$

FLOW RATE ANALYSIS, cont.

Friction Factors:
Since the velocities are not known, the values of Re are unknown and therefore the friction factors must be found iteratively. For initial values, assume flow is fully developed turbulent flow[2]. Friction factors found using Moody diagram referenced above.

A: $\varepsilon_A/D_A = 0$; $f_A = 0.008$
B: $\varepsilon_B/D_B = .0024$; $f_B = 0.023$
C: $\varepsilon_C/D_C = .0048$; $f_C = 0.028$

Air properties:

$T_{air} = 20^0$ C	$T_{air} = 200^0$ C
$\gamma = 11.81$ N/m^3	$\gamma = 7.317$ N/m^3
$\mu = 1.82 \times 10^{-5}$ N*s/m^2	$\mu = 2.53 \times 10^{-5}$ N*s/m^2
$\nu = 1.51 \times 10^{-5}$ m^2/s	$\nu = 3.39 \times 10^{-5}$ m^2/s

Define section I as section from pressure gage to start of tee (serial pipe flow):

$Q_A = Q_B = Q_I$
$h_{LI} = h_{LA} + h_{LB}$

Q = Flow rate
h = Head loss

Define sections II and III as from the tee to point 2 and point 3, respectively (parallel pipe flow):

$$Q_I = Q_{II} + Q_{III}$$
$$h_{LII} = h_{LIII} \qquad (1)$$

Head losses: (Path 1-2):

$$h_{LI} = \left(\frac{f_A L_A}{D_A} + \sum K_{LA} \right) \frac{V_A^2}{2g} + \left(\frac{f_B L_B}{D_B} + \sum K_{LB} \right) \frac{V_B^2}{2g}$$
$$Q_A = Q_B = V_A A_A = V_B A_B$$
$$V_B = V_A \left(\frac{A_A}{A_B} \right) = 4V_A$$

[2] Janna, W. Introduction to Fluid Mechanics. 3rd ed. PWS-Kent Publishing Co. (1993) p.242

FLOW RATE ANALYSIS, cont.

$$h_{LI} = \left(\frac{f_A L_A}{D_A} + \sum K_{LA} \right) \frac{V_A^2}{2g} + \left(\frac{f_B L_B}{D_B} + \sum K_{LB} \right) \frac{16 V_A^2}{2g}$$

$$h_{LI} = V_A^2 \left(\frac{(f_A)240 + 0.8 + 16\left((f_B)20 + 0.65\right)}{2g} \right) \tag{2}$$

$$h_{LII} = \left(\frac{f_C L_C}{D_C} + \sum K_{LC(1-2)} \right) \frac{V_{II}^2}{2g} = V_{II}^2 \left(\frac{(f_c)10 + 3.19}{2g} \right) \tag{3}$$

$$h_{LII} = h_{LIII}$$

$$\left(\frac{f_C L_{CII}}{D_C} + \sum K_{LC(1-2)} \right) \frac{V_{II}^2}{2g} = \left(\frac{f_C L_{CIII}}{D_C} + \sum K_{LC(1-3)} \right) \frac{V_{III}^2}{2g}$$

$$\left((f_c)10 + 3.19\right) V_{II}^2 = \left((f_c)16 + 2.69\right) V_{III}^2$$

$$V_{III} = \sqrt{\frac{\left((f_c)10 + 3.19\right) V_{II}^2}{\left((f_c)16 + 2.69\right)}} \tag{4}$$

Energy Equation for conduit flow between two points:

$$\frac{p_1}{\gamma} + \frac{V_1^2}{2g} + z_1 = \frac{p_2}{\gamma} + \frac{V_2^2}{\gamma} + z_2 + h_{LI} + h_{LII} \tag{5}$$

From the assumptions, system description:
p_1 = pressure gage; $p_2 = 0$
$V_1 = V_A$; $V_2 = 0$; z_1-$z_2 = 0$

$$\frac{p_1}{\gamma} + \frac{V_I^2}{2g} = h_{LI} + h_{LII} \tag{6}$$

Substituting expressions (2), (3) into (6) and rearranging:

$$\frac{p_1}{\gamma} + \frac{V_I^2}{2g} = V_I^2 \left(\frac{(f_A)240 + 0.8 + 16\left((f_B)20 + 0.65\right)}{2g} \right) + V_{II}^2 \left(\frac{(f_c)10 + 3.19}{2g} \right)$$

FLOW RATE ANALYSIS, cont.

$$V_I^2\left(1-\left(f_A\right)240+0.8+16\left(\left(f_B\right)20+0.65\right)\right)=V_{II}^2\left(\left(f_c\right)10+3.19\right)-\frac{2gp_1}{\gamma}$$

$$V_I=\sqrt{\frac{V_{II}^2\left(\left(f_c\right)10+3.19\right)-\frac{2gp_1}{\gamma}}{\left(1-\left(f_A\right)240+0.8+16\left(\left(f_B\right)20+0.65\right)\right)}} \qquad (6)$$

From (1):

$$Q_I=Q_{II}+Q_{III}$$
$$A_IV_I=A_{II}V_{II}+A_{III}V_{III} \qquad A_{II}=A_{III}$$
$$V_I=\left(V_{II}+V_{III}\right)\frac{A_{II}}{A_I}$$

Substituting the expressions from (4) yields:

$$V_I=\left(V_{II}+\sqrt{\frac{\left(\left(f_c\right)10+3.19\right)V_{II}^2}{\left(\left(f_c\right)16+2.69\right)}}\right).0624$$

$$V_I=V_{II}\left(1+\sqrt{\frac{\left(\left(f_c\right)10+3.19\right)}{\left(\left(f_c\right)16+2.69\right)}}\right).0624 \qquad (7)$$

Subtracting (7) from (6) gives the expression:

$$\sqrt{\frac{V_{II}^2\left(\left(f_c\right)10+3.19\right)-\frac{2gp_1}{\gamma}}{\left(1-\left(f_A\right)240+0.8+16\left(\left(f_B\right)20+0.65\right)\right)}}-V_{II}\left(1+\sqrt{\frac{\left(\left(f_c\right)10+3.19\right)}{\left(\left(f_c\right)16+2.69\right)}}\right).0624=0$$

The root of this expression can be solved on a scientific calculator to find V_{II} (which is the velocity in tube C), which can then be used to find the other velocities.

FLOW RATE ANALYSIS, cont.

Case 1: p_1 = 10.34 kPa, T_{air} = 20^0 C:

Iteration	Friction Factor	Velocities	Re	New Friction Factors
1	f_A = .008 f_B = .023 f_C = .028	V_A = 9.4 m/s V_B = 37.61 m/s V_C = 73.45 m/s	Re_A = 7905 Re_B = 15816 Re_C = 15355	f_A = .034 f_B = .032 f_C = .034
2	f_A = .034 f_B = .032 f_C = .034	V_A = 9.23 m/s V_B = 36.93 m/s V_C = 72.37 m/s	Re_A = 7905 Re_B = 15530 Re_C = 15216	f_A = .034 f_B = .032 f_C = .034

Approximate exit flow rate:

$$Q_{II} = Q_E$$

$$Q_E = A_{II} V_{II}$$

$$Q_E = \left(7.91 \times 10^{-7} \cdot m^2\right)\left(72.37 \cdot \frac{m}{s}\right)$$

$$Q_E = 5.72 \times 10^{-5} \cdot \frac{m^3}{s}$$

To see how the air properties affect the flow rate, this analysis was run using the air properties given above for 200^0 C.

Case 2: p_1 = 10.34 kPa, T_{air} = 200^0 C:

Iteration	Friction Factor	Velocities	Re	New Friction Factors
1	f_A = .034 f_B = .032 f_C = .034	V_A = 11.73 m/s V_B = 46.94 m/s V_C = 91.94 m/s	Re_A = 4394 Re_B = 8792 Re_C = 8610	f_A = .038 f_B = .036 f_C = .026
2	f_A = .038 f_B = .036 f_C = .026	V_A = 11.90 m/s V_B = 47.62 m/s V_C = 92.89 m/s	Re_A = 7905 Re_B = 8919 Re_C = 8699	f_A = .038 f_B = .036 f_C = .026

FLOW RATE ANALYSIS, cont.

$$Q_{II} = Q_E$$

$$Q_E = A_{II} V_{II}$$

$$Q_E = \left(7.91 \times 10^{-7} \cdot m^2\right)\left(92.89 \cdot \frac{m}{s}\right)$$

$$Q_E = 7.34 \times 10^{-5} \cdot \frac{m^3}{s}$$

These values differ by roughly 20%. Given that working with the Moody diagram generally yields 10% accuracy at best[3], this difference was deemed acceptable in terms of approximating the exit flow rate.

Case 3: p_1 = 20.68 kPa, T_{air} = 20^0 C

Iteration	Friction Factor	Velocities	Re	New Friction Factors
1	f_A = .034 f_B = .032 f_C = .034	V_A = 13.01 m/s V_B = 52.05 m/s V_C = 102.0 m/s	Re_A = 10942 Re_B = 21888 Re_C = 21447	f_A = .038 f_B = .030 f_C = .034
2	f_A = .038 f_B = .030 f_C = .034	V_A = 12.96 m/s V_B = 51.86 m/s V_C = 101.62 m/s	Re_A = 10900 Re_B = 21808 Re_C = 21367	f_A = .038 f_B = .030 f_C = .034

$$Q_{II} = Q_E$$

$$Q_E = A_{II} V_{II}$$

$$Q_E = \left(7.91 \times 10^{-7} \cdot m^2\right)\left(101.62 \cdot \frac{m}{s}\right)$$

$$Q_E = 8.03 \times 10^{-5} \cdot \frac{m^3}{s}$$

---

[3] Munson, Young, & Okiishi. Fundamentals of Fluid Mechanics. 4th ed. John Wiley & Sons. (2002) p.478.